

Improving volume-averaged simulations of matrix-stabilized combustion through direct X-ray μ CT characterization: Application to NH_3/H_2 -air combustion

Thorsten Zirwes^{a,b,c,*}, Guillaume Vignat^{a,**}, Edna R. Toro^a, Emeric Boigné^a, Khaled Younes^a, Dimosthenis Trimis^c, Matthias Ihme^{a,d}

^a*Department of Mechanical Engineering, Stanford University, Stanford CA 94305, USA*

^b*Steinbuch Centre for Computing, Karlsruhe Institute of Technology, Herrmann-von-Helmholtz-Platz 1, Eggenstein-Leopoldshafen 76344, Germany*

^c*Engler-Bunte-Institute, Division of Combustion Technology, Karlsruhe Institute of Technology, Engler-Bunte-Ring 1, Karlsruhe 76131, Germany*

^d*Department of Photon Science, SLAC National Accelerator Laboratory, Menlo Park, CA 94025, USA*

Abstract

Porous media combustion (PMC) relies on internal heat recirculation in an open-cell ceramic foam matrix to enhance the flame speed of fuels with poor combustion properties. Volume-averaged simulations are often used to study the combustion performance and pollutant emissions of such systems. However, due to the varying complexity of matrix geometries found in practical burners, as well as the wide range of closure models for the constitutive relations of the solid phase, contradicting statements about the predictive accuracy of these volume-averaged models can be found in the literature. In this work, we propose an open-source modeling framework for accurate volume-averaged PMC simulations by using first-principles methods to determine effective properties used in closure models. This framework relies on adequately characterizing the topology of the solid matrix, using commonly available X-ray computed microtomography. With this approach, significant improvements in accuracy are reported compared to empirical models from the literature. The framework based on first-principle evaluations of constitutive relations is compared against experimental measurements conducted on an interface-stabilized burner operated with premixed NH_3/H_2 -air. The model shows good agreement for exhaust gas composition and stability limits. The proposed simulation framework performs significantly better than state-of-the-art techniques that employ commonly used empirical correlations for effective matrix properties.

Keywords: Matrix stabilized combustion, volume-averaged modeling, ammonia combustion, X-ray computed microtomography

Novelty and Significance Statement

We present a new open-source simulation framework for improved characterization of porous media combustion. By utilizing μ CT techniques, accurate effective matrix properties can be determined from first-principle simulations. These effective properties are used in closure models for 1D volume-averaged reacting flow simulations using appropriate sub-models for heat recirculation. This modeling framework is able to reliably predict stability limits while conventional closure models yield erroneous trends. Assessment of the resulting modeling framework is performed using experiments with exhaust gas characterization performed on a NH_3/H_2 -air porous media burner.

Authors Contributions

TZ: conceptualization, methodology, investigation, software, validation, writing - original draft; GV: conceptualization, methodology, investigation, data curation, writing - original draft; ET: investigation, data curation, writing - review; EB: conceptualization, methodology, writing - review; KY: investigation; DT: supervision, funding acquisition; MI: conceptualization, methodology, investigation, supervision, project administration, funding acquisition, writing - review & editing.

1 **Introduction**

The transition towards low-carbon combustion devices is a promising solution to reduce net greenhouse gas emissions. Low-carbon fuels such as hydrogen (H_2), ammonia (NH_3), and low-heating-value syngas and biogas are therefore subjects of active research. However, most of these fuels exhibit poor combustion properties, making it difficult to stabilize flames in conventional combustion devices [1–3]. One solution is the use of porous media combustion (PMC) [4–6]. These burners consist of an open-cell ceramic matrix. Heat recirculation

*Currently at the Institute for Combustion Technology, University of Stuttgart, Pfaffenwaldring 31, Stuttgart 70569, Germany

**Corresponding author: gignat@stanford.edu

8 to the reaction zone by conduction and radiation within the solid matrix can significantly
9 increase the flame speed. This is helpful to stabilize combustion processes when using fuels
10 with poor combustion properties [7–12].

11 Numerical simulations of PMC can assist with understanding, designing, and optimizing
12 porous media burners (PMBs) [4, 6, 13]. Different simulation concepts have been developed
13 to model PMC, including pore-resolved simulations and volume-averaged methods. Direct
14 pore-level simulations (DPLS) generally couple a 3D fully resolved finite-volume reacting flow
15 simulation with a 3D thermal simulation of the solid. DPLS can yield accurate results, but
16 they require the full resolution of the flame structure and of radiative and diffusive transport
17 in the complex pore topology [14–16]. This stringent requirement makes their computational
18 cost and complexity high, typically limiting their application beyond fundamental research.

19 In contrast, volume-averaged methods are a popular concept for low-order simulations
20 of PMC. In particular, 1D volume-averaged simulations (1D–VAS) describe the 1D flame
21 structure in porous media and are frequently employed in practical applications. While the
22 computational cost is low, these simulations require appropriate closure models to describe
23 the solid phase, the inter-phase heat transfer, and other constitutive properties. This re-
24 quires the accurate determination of effective properties accounting for effects of the solid
25 geometry [15, 17]. The present work focuses on 1D–VAS and their ability to capture en-
26 gineering quantities of interest, such as stability limits and pollutant emissions. In what
27 follows, we will briefly review modeling approaches typically used in 1D–VAS.

28 Lawson and Norbury [18] performed one of the first 1D–VAS for porous media applica-
29 tions, and since then, conflicting reports about the predictive capabilities of volume-averaged
30 simulations have been published [6]. For example, in [17, 19–23], the authors have reported
31 good agreement between 1D–VAS and reference data. By contrast, in [24–30], 1D–VAS were
32 unable to reproduce experimental measurements. These studies cover a large range of burner
33 configurations, from open-cell ceramic foam burners, to filtration combustion and packed bed
34 reactors, with applications ranging from gas-turbine combustors, heat production in process
35 burners, to fuel reforming and hydrogen production. The aforementioned studies highlight
36 that the predictive capability of 1D–VAS for matrix-stabilized combustion heavily depends on

37 the choice of closure models for inter-phase heat transfer, tortuosity, and heat transport by
38 conduction and radiation within the solid matrix. These studies also indicate that 1D-VAS
39 have a strong sensitivity to effective solid matrix properties. Therefore, direct and accurate
40 measurements of these properties tend to yield more predictive 1D-VAS.

41 Radiative heat transfer is one of the dominant processes of heat recirculation in the solid
42 matrix, and is among the closure models that has received the most attention for PMC
43 modelling [6]. The Rosseland model is a popular approach for modeling radiative transport
44 [18, 19, 24, 29, 31, 32]. It relies on modeling radiative processes in the solid as an effec-
45 tive heat conduction coefficient. However, this model has been shown to yield considerable
46 discrepancies when compared with experimental measurements [6]. Nonetheless, it is still
47 commonly used today for its simple implementation. The P3 model is another approach,
48 proposed by Barra et al. [25] and Henneke and Ellzey [33], who applied it to low velocity
49 filtration combustion. It approximates the solution of the radiation transport equation us-
50 ing an analytical ansatz function. Another approach is to directly solve the full radiation
51 transport equation (RTE). This approach is accurate, but also significantly more compu-
52 tationally intensive [22, 34]. The Schuster-Schwarzschild model [35], successfully used by
53 Sobhani et al. [17, 23], is a cost-effective alternative to solving the full RTE for conditions
54 in which the solid can be assumed to be a gray body. It relies on solving a set of coupled
55 ordinary differential equations to compute the two components of the axial radiative flux.
56 The effect of the solid geometry is incorporated using effective radiative properties, which
57 can be computed a-priori using inexpensive ray-tracing simulations.

58 Solid heat conduction of the matrix is another important process for heat recircula-
59 tion and flame stabilization. The determination of effective heat conduction properties for
60 volume-averaged simulations requires both a good characterization of the bulk material's
61 property, which is often lacking for high temperature engineered ceramics used in PMBs
62 [36], and a good model to account for the effect of the solid matrix' macroporosity. Con-
63 cerning the latter, a simplified approach in which the material conductivity is multiplied by
64 the volume fraction of the solid inside the control volume is sometimes used [37–39]. Depend-
65 ing on the geometry of the solid, the actual effective value can differ significantly [36, 40].

66 A better estimate can be obtained by performing additional thermal simulations using the
67 geometry of the solid structure. This can be obtained using a thermal finite volume solver on
68 a geometrical grid obtained from x-ray micro-computed-tomography (μ CT) [15, 17, 36, 41].

69 In addition to heat recirculation within the solid matrix, other physical phenomena have
70 to be considered for 1D-VAS, namely inter-phase heat transfer, gas-phase tortuosity, and
71 flame wrinkling. Heat transfer between the solid and the gas phase is usually modeled with
72 a volumetric heat transfer coefficient, derived from Nusselt number correlations dependent on
73 the flow regime and the solid geometry. These correlations are most often determined from
74 non-reactive flows using either experimental measurements or DPLS [17, 19, 29, 39, 42–49].
75 The porous matrix also affects diffusive processes in the gas phase by increasing characteristic
76 transport length scales, a phenomena known as tortuosity. This can be taken into account
77 by decreasing the diffusion coefficients found in the 1D-VAS governing equations for gas-
78 phase temperature and species [50]. In practice, the effect of tortuosity for combustion
79 applications in PMBs is often neglected [17, 22]. While different correlations exist that
80 relate tortuosity to pore size, porosity, or Péclet number [20, 25, 26, 42, 46, 51], their
81 validity is often limited. Alternatively, effective tortuosity properties can be computed from
82 high resolution tomographic images of the solid matrix [19, 29, 52]. In recent years, new
83 correlations have also been derived using machine learning approaches [53, 54]. Table 1
84 presents a synthesis of closure models commonly employed in 1D-VAS.

85 In this work, we present a framework for 1D-VAS. We hypothesize that the reliability of
86 1D-VAS can be improved by utilizing accurate effective properties for closure models. With
87 modern tools such as ceramic additive manufacturing and μ CT [36], the detailed macro-
88 porous structure of the ceramic matrix is often readily accessible and can be utilized to
89 accurately derive these effective properties by performing separate, inexpensive 3D simula-
90 tions based on first-principles. These effective properties can then be utilized to perform
91 1D-VAS reacting flow simulations. We refer to this approach as the 1D-VAS-FP framework
92 (1D Volume-Averaged Simulations with closure models derived from First Principles).

93 In the present work, we introduce an open-source tool-chain that implements the 1D-
94 VAS-FP framework and applies it to a foam geometry characterized using high-resolution

Table 1: Literature review on closure models used in 1D-VAS for PMBs. The models indicated **in bold** are those used in the 1D-VAS-FP framework described in the present work. Those *in italic* are used in the 1D-VAS-EMP framework employed as a reference in the present work.

Physical process	Modeling approach	Reference
Solver adapted from	Chemkin (closed source)	[19, 20, 26, 29, 33, 34, 51]
	Cantera (closed source)	[15, 17, 32]
	Cantera (open-source)	present work
Chemical mechanism	Reduced	[27]
	Detailed	[15, 17, 19, 20, 22, 26, 51], present work
Radiation	<i>Rosseland model</i>	[18, 19, 24, 29, 31, 32]
	P3	[25, 26, 33]
	Schuster-Schwarzschild	[17, 23]
	Schuster-Schwarzschild with properties from μCT	present work
	Full Radiative Transfer Equation	[22, 34]
Solid heat conduction	<i>Derived from porosity</i>	[22, 24, 26, 27, 32, 37–39, 51]
	3D simulations from μCT	[15, 17, 19, 29, 40, 41, 55], present work
Inter-phase heat transfer	<i>Derived from non-reacting experiments/DPLS</i>	[17, 22, 24, 26, 27, 29, 31, 39, 42–49], present work
	Derived from reacting experiments/DPLS	[15, 29]
Gas-phase diffusion	<i>Neglected</i>	[17, 22]
	Tortuosity from correlation	[20, 25, 26, 42, 46, 51]
	3D simulation from μCT	[15, 19, 29], present work

95 μ CT. The closure models used in our implementation of the 1D-VAS-FP framework are
96 highlighted in bold font in Table 1. The test case for the evaluation of the 1D-VAS-FP
97 framework is an interface-stabilized PMB, described in Section 2, that was recently stud-
98 ied in [56]. Matrix-stabilized premixed NH_3/H_2 -air combustion was studied over a wide
99 range of operating conditions and fuel mixture compositions. The 1D-VAS-FP framework
100 and tool-chain are introduced and described in detail in Section 3. Results are presented
101 in Section 4.1, which assesses the ability of 1D-VAS-FP simulations to accurately capture
102 the stability limit of the burner. To provide a comparative reference, 1D-VAS simulations
103 are also conducted using state-of-the-art empirical closure models and correlations. This
104 is thereafter referred to as the 1D-VAS-EMP framework (1D Volume-Averaged Simulations
105 with EMPirical closure models). In Table 1, closure models used for 1D-VAS-EMP simula-
106 tions are indicated using italic. 1D-VAS-FP and 1D-VAS-EMP are compared in Section 4.2.
107 The focus is then placed on pollutant emissions: we first assess the accuracy of the 1D-
108 VAS-FP framework by comparing with experiments in Section 4.3. In Section 4.4, we focus
109 on a more fundamental analysis of PMB-stabilized NH_3 combustion using insights from
110 1D-VAS-FP simulations. Conclusions are presented in Section 5.

111 2. Experimental setup, instrumentation, and measurements

112 The experimental measurements used in the present work were published in [56], and
113 we refer the reader to this reference for a more detailed description of the experimental
114 setup. The burner is of an interface-stabilized design, with three axially staged sections. It
115 has an outer diameter of 50.8 mm. The perfectly premixed reactants first flow through two
116 blocks of 25.4 mm-long 40 pores per inch (PPI) open-cell yttria-stabilized zirconia alumina
117 (YZA, with 2% calcium oxide, 2% yttria, 62% zirconia, and 34% alumina by mass) foam
118 manufactured by Selee (Hendersonville, NC, USA), acting as flame arrestor. These blocks
119 are followed by two 25.4 mm-long blocks of SiC foams manufactured by Ultramet (Pacoima,
120 CA, USA). The first of these two blocks has a larger pore size (3 PPI) than the second
121 (10 PPI). The burner is designed such that combustion occurs within these SiC ceramic
122 foams [5]. Note that the PPI ratings used to describe these ceramic foams are a commercial

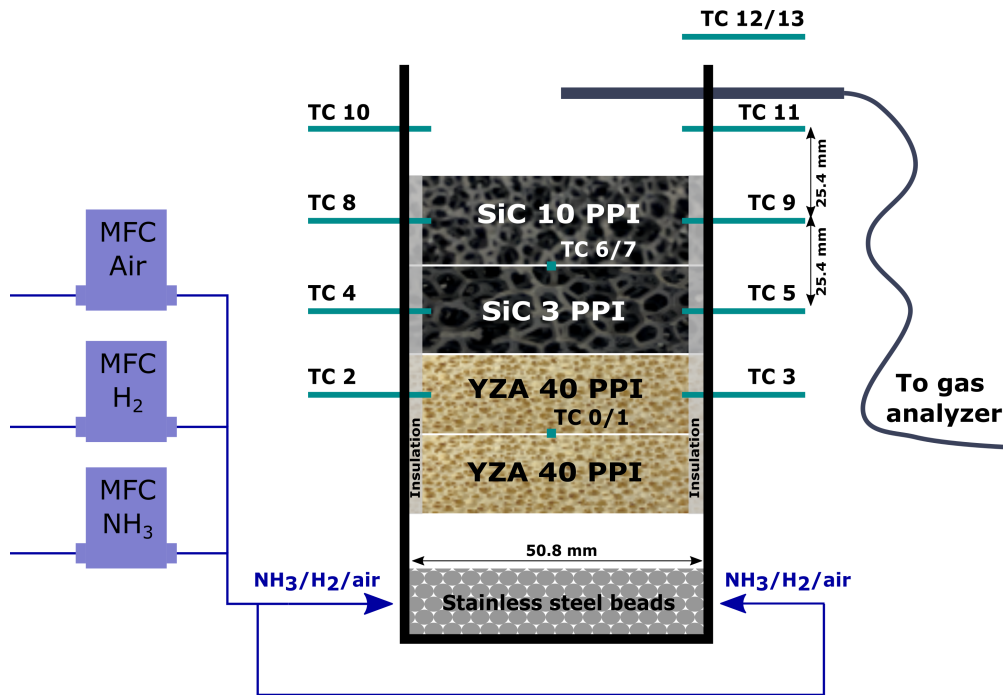


Figure 1: Schematic of the experimental apparatus (not to scale). MFC: mass flow controller; SiC: silicon carbide; YZA: yttria-stabilized zirconia alumina; TC: thermocouple. Reproduced from [56].

123 designation.

124 The flow of reactants is controlled by mass flow controllers (Alicat, Tucson, AZ, USA) and
 125 all reactants are premixed upstream of the burner's inlet. The uncertainties on the reported
 126 equivalence ratios and mass flow rates are 1.6% and 0.8%, respectively. The experiments are
 127 conducted at ambient pressure and temperature. Gas analysis is performed in the exhaust
 128 of the burner. NO, O₂, NH₃, and H₂ concentrations are reported in dried exhaust gases. NO
 129 and NH₃ emissions are normalized to 15% O₂ following standard practice [57]. Experimental
 130 uncertainties on these measurements are 20 %, 15 % and 7 %, respectively, for normalized
 131 NO, normalized NH₃ and H₂, respectively [56].

132 3. 1D modeling framework

133 3.1. Governing equations and constitutive relations

134 In the present work, we consider a PMB with constant cross-section and an axial flow
135 direction represented with coordinate x . In this model, we invoke the following assumptions:

- 136 i. The solid phase is chemically inert with no catalytic effects,
- 137 ii. Radiation within the gas phase and between the solid and gas is negligible,
- 138 iii. Dufour and Soret effects are negligible,
- 139 iv. Viscous dissipation is negligible,
- 140 v. The flow has a variable density, but can be treated as incompressible,
- 141 vi. The axial pressure gradient within the burner has negligible effects on the chemistry,
142 and on heat and species transport, and
- 143 vii. Turbulent effects are negligible given the low Reynolds number of the flow.

The 1D volume-averaged governing equations comprise the balance equations for mass, species, and temperature of the gas phase as [17, 22, 29, 58]

$$\frac{\partial(\rho_g \varepsilon_v)}{\partial t} + \frac{\partial}{\partial x} (\varepsilon_v \rho_g u) = 0, \quad (1)$$

$$\frac{\partial(\rho_g \varepsilon_v Y_k)}{\partial t} + \frac{\partial}{\partial x} (\varepsilon_v \rho_g Y_k u) = - \frac{\partial}{\partial x} (\varepsilon_v j_k) + \varepsilon_v \dot{\omega}_k, \quad (2)$$

$$c_{p,g} \frac{\partial(\rho_g \varepsilon_v T_g)}{\partial t} + c_{p,g} \frac{\partial}{\partial x} (\varepsilon_v \rho_g T_g u) = \frac{\partial}{\partial x} \left(\varepsilon_v \frac{\lambda_g}{\eta} \frac{\partial T_g}{\partial x} \right) - \varepsilon_v \left(\sum_{k=1}^{N_s} c_{p,k} j_k \right) \frac{\partial T_g}{\partial x} - h_v (T_g - T_s) + \varepsilon_v \dot{q}_{\text{chem}}, \quad (3)$$

144 where the subscripts g and s denote the gas and solid phase, respectively, ρ is the density, ε_v
145 is the porosity, u is the interstitial axial velocity, Y_k is the mass fraction of the k^{th} species,
146 j_k is its diffusive mass flux, and $\dot{\omega}_k$ is its reaction rate. T is the temperature, c_p the isobaric
147 heat capacity of the mixture, $c_{p,k}$ the isobaric heat capacity of the k^{th} species, N_s is the
148 number of species, λ the gas-phase heat conductivity, η is the tortuosity factor, h_v is the
149 volumetric inter-phase heat transfer coefficient, and \dot{q}_{chem} is the heat release rate associated
150 with chemical reactions.

In the gas phase, the diffusive mass flux of each species j_k in Eq. (2) is modeled with the Curtiss-Hirschfelder approximation and includes tortuosity effects [59]:

$$j_k = -\rho_g \frac{M_k}{M} \frac{D_k}{\eta} \frac{\partial X_k}{\partial x} + Y_k \rho_g \sum_{i=1}^{N_s} \frac{M_i}{M} \frac{D_i}{\eta} \frac{\partial X_i}{\partial x}, \quad (4)$$

where M_k is the molar mass of the k^{th} species, D_k its diffusion coefficient, and M is the mean molecular weight. Heat transfer between solid and gas phase is modeled by a volumetric heat transfer coefficient h_v , which is computed as [29]

$$h_v = Nu \frac{S_v \lambda_g}{d_h}, \quad (5)$$

where S_v is the specific surface of the porous matrix and $d_h = 4\varepsilon_v/S_v$ is the hydraulic diameter of the porous medium. The Nusselt number, Nu , is computed from the correlation by Bedoya et al. [29]

$$Nu = 3.7 Re^{0.38} Pr^{0.25}, \quad (6)$$

with the Reynolds and Prandtl numbers based on the gas-phase properties

$$Re = \frac{\rho_g u d_h}{\mu_g}, \quad Pr = \frac{c_{p,g} \mu_g}{\lambda_g}, \quad (7)$$

151 where μ_g is the viscosity of the gas phase.

The governing equation for the solid-phase temperature T_s is

$$(1 - \varepsilon_v) \rho_s c_s \frac{\partial T_s}{\partial t} = \frac{\partial}{\partial x} \left(\lambda_{\text{eff}} \frac{\partial T_s}{\partial x} \right) - \dot{q}_{\text{rad}} - \dot{q}_{\text{loss}} + h_v (T_g - T_s), \quad (8)$$

152 where c_s is the heat capacity of the solid, λ_{eff} is the effective heat conductivity, \dot{q}_{rad} is the
153 radiative heat transfer source term, and \dot{q}_{loss} is the source term for heat losses through the
154 outer radial boundary of the burner.

Heat recirculation due to radiation is an essential process to describe interface-stabilized PMC. Under a gray body assumption, we model axial heat transport by radiation with the Schuster-Schwarzschild model [17, 23, 35], where \dot{q}_{rad} in Eq. (8) is computed from the contribution of radiative flux in positive axial direction \dot{q}_{R}^+ and negative axial direction \dot{q}_{R}^- ,

$$\dot{q}_{\text{rad}} = 2\beta(1 - \omega_{\text{rad}})(2\sigma T_s^4 - [\dot{q}_{\text{R}}^+ + \dot{q}_{\text{R}}^-]), \quad (9)$$

where σ is the Stefan–Boltzmann constant. The extinction coefficient β is directly computed from the μ CT scans. The scattering albedo ω_{rad} is computed using a gray body assumption as [60, 61]

$$\omega_{\text{rad}} = \frac{1}{2} (2 - e_{\text{rad}}), \quad (10)$$

155 where e_{rad} is the emissivity of the solid surface.

To determine \dot{q}_{R}^+ and \dot{q}_{R}^- , two linear ordinary differential equations are solved [35]:

$$\frac{d\dot{q}^+}{dx} = -\beta(2 - \omega_{\text{rad}})\dot{q}^+ + \beta\omega_{\text{rad}}\dot{q}^- + 2\beta(1 - \omega_{\text{rad}})\sigma T_s^4, \quad (11)$$

$$-\frac{d\dot{q}^-}{dx} = -\beta(2 - \omega_{\text{rad}})\dot{q}^- + \beta\omega_{\text{rad}}\dot{q}^+ + 2\beta(1 - \omega_{\text{rad}})\sigma T_s^4. \quad (12)$$

In addition to the axial radiative heat transport, radial radiative heat loss through the outer insulation layer is taken into account as

$$\dot{q}_{\text{loss}} = \frac{4\sigma e_{\text{rad}}\tau}{D}(T_s^4 - T_{\text{amb}}^4). \quad (13)$$

156 In this 1D model, heat losses are represented as volumetric sources, assuming a cylindrical
 157 burner with an outer diameter D and transmissivity of the insulation layer τ . T_{amb} is
 158 the ambient temperature, here assumed to be 300 K. Heat losses due to conduction and
 159 convection on the outer cylindrical boundary of the burner are neglected in the present
 160 work, as they are estimated to be an order of magnitude smaller than losses due to radiative
 161 processes. The derivation of Eq. (13) and the estimation of convective heat losses are detailed
 162 in the supplementary materials.

163 The boundary conditions for the governing equations are summarized in Table 2.

164 In this work, we use the reaction mechanism proposed by Stagni et al. [62] for NH_3/H_2 -air
 165 combustion. This mechanism consists of 29 species and 203 reactions, and has been validated
 166 over a wide range of equivalence ratios and H_2 dilutions corresponding to the experimental
 167 conditions in [56]. A comparison with other reaction mechanisms [63, 64] is included in the
 168 supplementary materials.

169 3.2. Software architecture

170 Solving the governing equations requires both the determination of effective solid matrix
 171 properties and a numerical procedure for solving Eqs. (1)–(13). Therefore, we propose the

Table 2: Boundary conditions for 1D–VAS. [†] The outlet boundary condition for T_s models the radiative heat flux from the top solid surface of the burner to the ambience. Heat losses to the ambience on the outer cylindrical boundary of the burner are modeled using a volumetric source term, Eq. (13).

Quantity	Inlet	Outlet
u	fixed	zero gradient
Y_k	fixed mass flux	zero gradient
T_g	300 K	zero gradient
T_s	300 K	$\lambda_{\text{eff}} \frac{\partial T_s}{\partial x} + e_{\text{rad}} \sigma (1 - \varepsilon_v) (T_s^4 - T_{\text{amb}}^4) = 0^\dagger$
\dot{q}^+	σT_{amb}^4	—
\dot{q}^-	—	σT_{amb}^4

172 1D–VAS–FP framework, a combination of first-principles-based methods for the determina-
173 tion of effective properties and conventional 1D flame modeling software. This framework is
174 summarized in Fig. 2 and utilizes open-source software. Section 3.3 describes the determi-
175 nation of effective matrix properties using first-principle methods. Section 3.4 discusses the
176 numerical implementation of the steady-state solver for governing equations, Eqs. (1)–(3)
177 and Eq. (8).

178 3.3. Determination of effective matrix properties

179 The governing equations introduced in Section 3.1 include a number of submodels that
180 rely on effective macroporous solid properties to account for 3D effects of the porous matrix.
181 These properties are listed in blue at the center of Fig. 2. To determine these properties, the
182 ceramic foams used in the present work were characterized using 3D tomographic images
183 obtained using μ CT performed on a Zeiss Xradia Versa 520 x-ray microscope (Carl Zeiss
184 Microscopy GmbH, Jena, Germany). The acquisition parameters for the scans are reported
185 in Table 3. After acquisition, the images were denoised using a high-frequency despeckling
186 filter and a non-linear edge preserving filter [67]. Segmentation of the solid and gaseous
187 phases was performed using the method proposed by Otsu [68]. As a final pre-processing

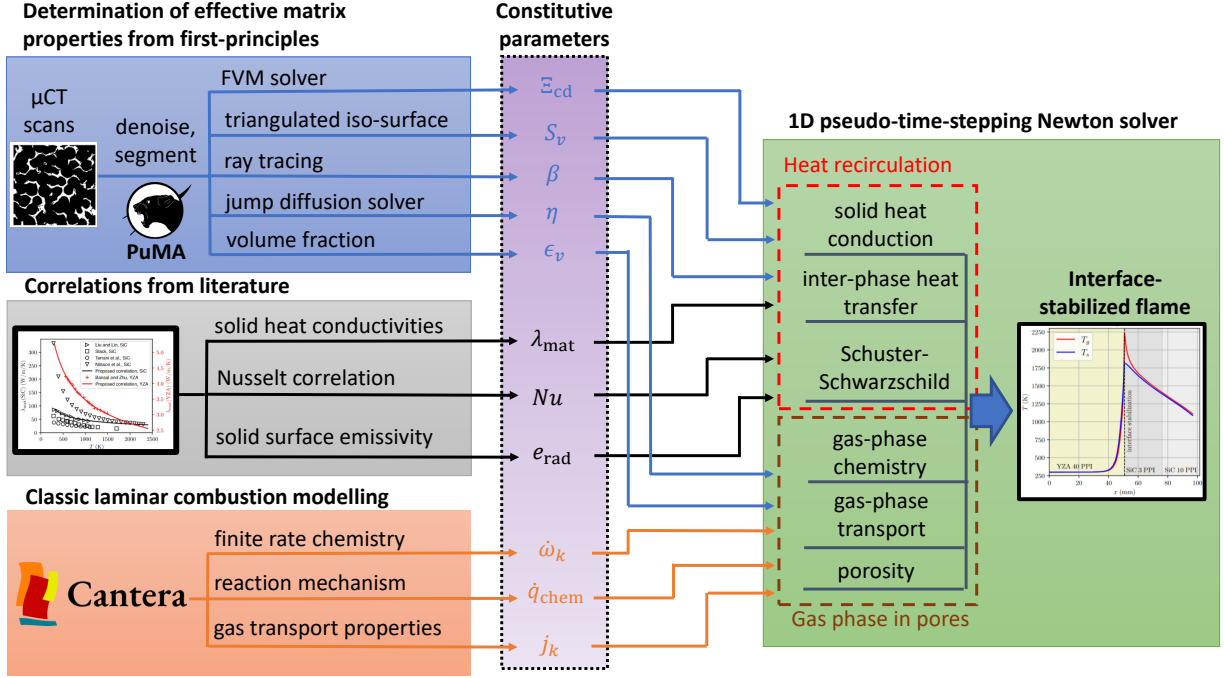


Figure 2: Summary of the proposed 1D-VAS-FP framework for predictive modeling of 1D volume-averaged simulations for combustion in porous media. All software mentioned above are open-source, including the 1D pseudo-time-stepping Newton solver (green), which is an open-source modification of Cantera [65], available at [66].

188 step, morphological closing was performed on the images. The resulting 3D models for the
 189 three porous foam segments are shown in Fig. 3. In addition to different pore sizes, the
 190 morphology of the ceramic lattice shows substantial differences between the YZA and SiC
 191 foams. Specifically, the SiC foams manufactured by Ultramet form a lattice of hollow struts,
 192 while the YZA foam from Selee has a larger solid structure, which, although pore sizes are
 193 similar, has a larger specific surface area.

The effective heat conductivity of the foams was calculated from the temperature-dependent bulk heat conductivity λ_{mat} of the material and an effective thermal conductivity factor Ξ_{cd} , which accounts for macroporosity effects and depends on the topology of the solid matrix

$$\lambda_{\text{eff}} = \lambda_{\text{mat}}(T_s) \Xi_{\text{cd}}. \quad (14)$$

Table 3: Acquisition parameters for the μ CT scans.

Description (units)	YZA	SiC	SiC
Image width (voxel)	2008	2009	2008
Image height (voxel)	2048	2048	2048
Images per scan	2026	2026	2024
Voxel size (μm)	26.4	26.4	25.9
Exposure (s)	3.0	3.0	3.0
x-ray tube voltage (kV)	140.0	60.0	60.0
x-ray tube intensity (mA)	71.0	83.0	83.0

Table 4: Coefficients for the heat conductivity correlations in Eq. (15).

Coefficient (units)	YZA	SiC
λ_s^{ref} ($\text{W m}^{-1} \text{K}^{-1}$)	91.5	5.33
a	-0.35	-0.53

Ξ_{cd} is determined from the μ CT scans using a finite volume heat transfer solver [69]. The thermal conductivity λ_{mat} of SiC strongly depends on its manufacturing process, with appreciable differences between mono-crystalline SiC obtained by chemical vapor deposition [70, 71] and hot pressing and sintering [72–74]. Experimental measurements of λ_{mat} are unfortunately not available for SiC manufactured using the vitreous carbon infiltration process used by our supplier. Measurements from [70–74] are reproduced in Fig. 4. In the present work, we use a correlation based on the data by Liu and Lin [72], whose samples had a similar microporosity to ours, and agrees well with the high-temperature results of Nilsson et al. [70]:

$$\lambda_{\text{mat}}(T_s) = \lambda_s^{\text{ref}} \left(\frac{T_s}{T_0} \right)^a \quad (15)$$

194 where $T_0 = 293 \text{ K}$ and the coefficients λ_s^{ref} and a are reported in Table 4. The thermal
 195 conductivity of YZA reported in the literature also presents strong variability. This is due
 196 to the large design range for the composition of these ceramic materials [75], as well as
 197 the strong dependency of YZA’s heat conductivity on grain size and microporosity [36, 76,

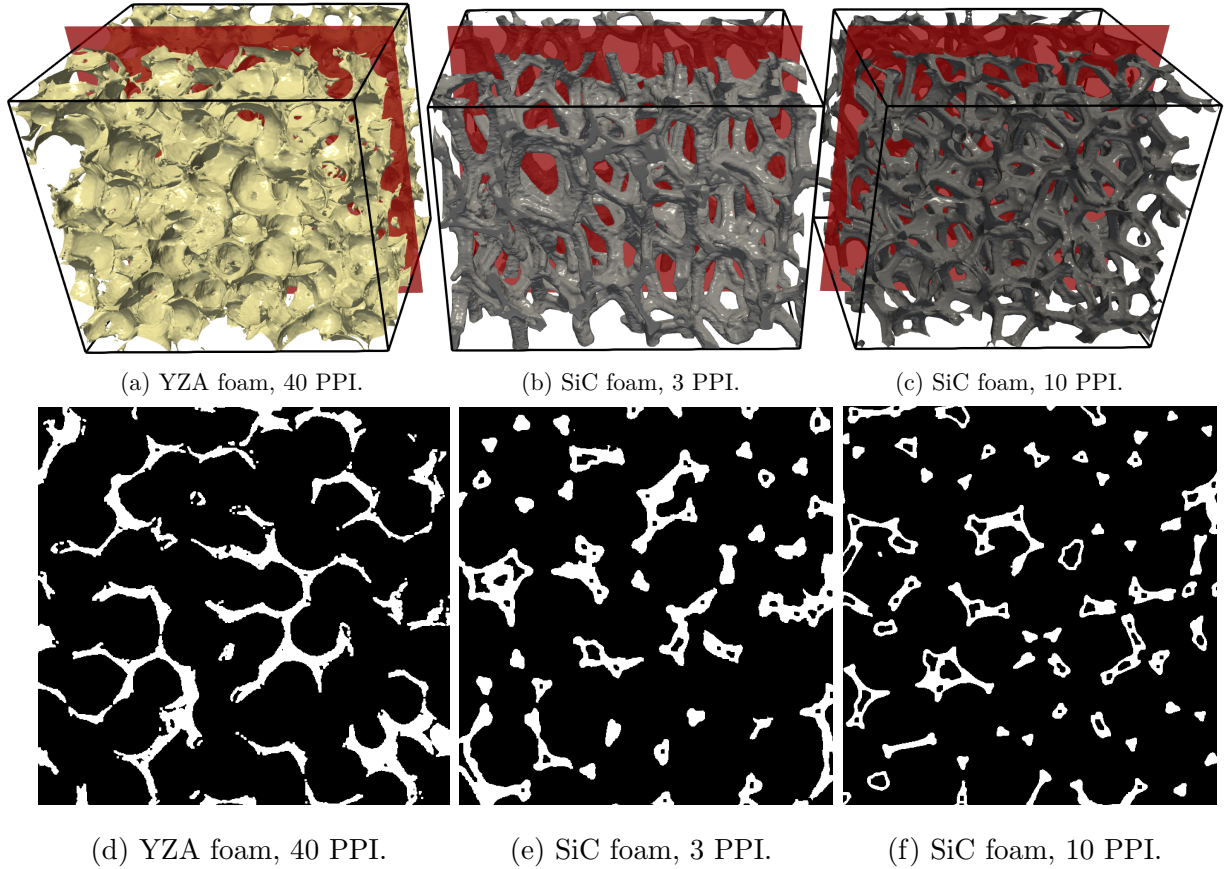


Figure 3: 3D renderings of the CT scans performed for the three different ceramic foams (a)–(c) used in the burner. Red planes show representative cutting planes, given in (d)–(f). White areas are the solid struts, black areas the open pore volume.

198 [77]. The correlations in Eq. (15) were derived from experimental measurements by Bansal
 199 and Zhu [75], which best matched the composition of the YZA used in our burner. Their
 200 measurements are also reproduced in Fig. 4.

201 With the exception of the thermal conductivity efficiency factor Ξ_{cd} , all properties com-
 202 puted from μ CT require that the hollow struts of the SiC foams are filled. This is ac-
 203 complished by isolating and filling void volumes that are not connected to the main flow
 204 channel using a connectivity tree search algorithm [41]. The porosity ε_v is then computed
 205 as the volume fraction of the void voxels. To compute the characteristic pore diameter (also
 206 known as window diameter) and cell diameter, we use a 3D distance transform watershed

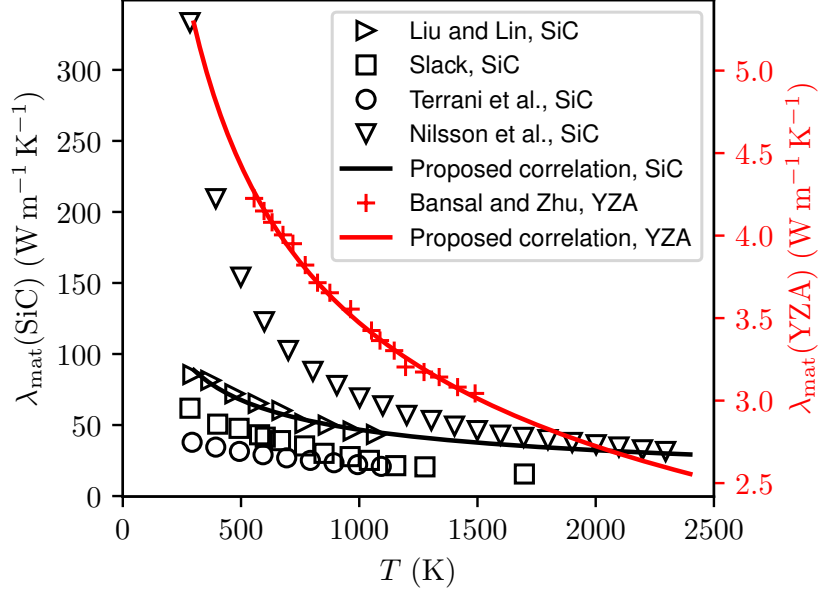


Figure 4: Experimental measurements of the heat conductivity of YZA and SiC and comparison with the correlation used in the present work, Eq. (15). Bansal and Zhu [75] characterized the heat conductivity of YZA, Liu and Lin [72] that of hot pressed sintered SiC, Slack and Nilsson et al. [70, 71] that of single crystal SiC, and Terrani et al. [73] that of 3D printed SiC. The black and red curves show the correlations used in the present work, Eq. (15), with parameters specified in Table 4.

algorithm followed by a particle analyzer, both implemented in the PoreSpy toolbox [78, 79]. The specific surface area S_v is computed using a triangulated isosurface approximation of the foam structure [41]. The effective solid density is calculated as $\rho_s = m_s / (\pi l r^2 (1 - \varepsilon_v))$, where m_s is the mass of a foam block, measured on a ZSP-500 scale (Scientech, Boulder, CO, USA), l is its thickness, and r is its radius.

The tortuosity factor η (Eqs. (3) and (4)) models the effect of the increased characteristic length scales of gas-phase diffusion caused by the foam geometry. η is obtained from the μ CT using the dedicated explicit jump solver of PuMA [52]. The values of η for the three burner segments are reported in Table 5.

The extinction coefficient β , which is usually determined from empirical models based

Table 5: Geometric characteristics and effective properties of the porous foams employed in the present work for simulations within the 1D–VAS–FP framework. †: values obtained using μ CT and in-house measurements; *: values obtained from the literature.

Description (unit)	YZA	SiC	SiC
Commercial designation (PPI)	40	3	10
Thickness l (mm)	50.8	25.4	25.4
Porosity ε_v (%)	82.5 [†]	86.2 [†]	86.0 [†]
Pore diameter d_p (mm)	1.11 [†]	1.56 [†]	1.07 [†]
Cell size d_c (mm)	2 [†]	3.2 [†]	2.6 [†]
Specific surface S_v (m^{-1})	1,592 [†]	934 [†]	986 [†]
Effective density ρ_s (g cm^{-3})	5.2 [†]	3.21 [†]	3.21 [†]
Material heat conductivity λ_{mat} ($\text{W m}^{-1} \text{K}^{-1}$)	Eq. (15) [*]	Eq. (15) [*]	Eq. (15) [*]
Axial thermal conductivity efficiency factor Ξ_{cd} (%)	7.2 [†]	5.1 [†]	4.3 [†]
Tortuosity factor η (m m^{-1})	1.34 [†]	1.17 [†]	1.15 [†]
Material emissivity e_{rad}	0.9 [*]	0.9 [*]	0.9 [*]
Extinction coefficient β (m^{-1})	1,340 [†]	526 [†]	683 [†]
Insulation transmissivity τ	0.6	0.6	0.6

217 on the pore diameter and porosity of the solid, is in this work directly calculated for each
218 burner section from ray tracing simulations using the geometry determined from μ CT. A
219 large number of point sources are randomly distributed in the void section of the foam. From
220 these points, rays are cast in random directions. The path length of each ray from the light
221 source to the nearest solid is recorded. With a sufficient number of rays and point sources,
222 the inverse mean distance of ray pathways converges to the extinction coefficient [69].

223 3.4. Numerical implementation and solution strategy

224 The governing equations and constitutive relations, Eqs. (1)–(13), were implemented in
225 Cantera [65] as an extension to its steady-state 1D reacting flow solver module. Since the
226 numerical methods used in Cantera are well documented [65, 80], we focus here on the

227 algorithmic extension to include PMC.

228 First, the gas-phase equations for the balance of total mass, species mass fractions, and
229 gas-phase temperature, Eqs. (1)–(3), are extended by adding the porosity ε_v and tortuosity
230 factor η , which are both a function of the axial coordinate x . All material and effective
231 properties can be assigned arbitrarily as a function of x in our implementation, which is well
232 suited to model the three section burner described in Sec. 2 and examined in Sec. 4. Note
233 that the gas-phase governing equations, Eqs. (1)–(3), are formulated to properly account
234 for spatially variable effective properties of the solid porous matrix. The inter-phase heat
235 transfer term is also added to the gas-phase temperature equation solved by Cantera.

236 Next, an equation for the temperature of the solid-phase is added and coupled to the gas
237 phase solver. The main numerical challenge is the large characteristic time scale associated
238 with the solid-phase temperature equation compared to the gas-phase equations [33]. In
239 addition, our implementation is capable of modelling burners with highly inhomogeneous
240 solid properties typically found in interface stabilized burners [5] and in burner designs
241 leveraging topology gradation [17]. For these reasons and to increase solver robustness, we
242 use a dedicated solution strategy implemented in our modified Cantera solver. A program
243 flow-chart is given in the supplementary materials, Fig. S1. After setting the initial con-
244 ditions, we solve for the solid-phase temperature T_s in the steady-state formulation while
245 keeping the gas-phase velocity u , temperature T_g , and species mass fractions Y_k constant.
246 For this step, Eigen’s [81] direct sparse solver based on supernodal LU factorization and
247 column approximate minimum degree ordering is employed. Next, the residual matrix for
248 the gas-phase governing equations is assembled. For this, the finite difference approach of
249 Cantera is used. A Newton iteration attempts to find a steady-state solution on the cur-
250 rent numerical grid. If the Newton step does not converge, a series of pseudo-time steps
251 is performed to find a better initial condition for the next Newton iteration. During both
252 the Newton and pseudo-time steps, the solid-phase temperature is fixed to decouple the gas
253 and solid time scales. Once a steady-state solution for the gas-phase properties is found, the
254 convergence between the solid-phase and gas-phase is checked. If the solid and gas-phase are
255 not converged, this coupled solution procedure is repeated. If both are converged, adaptive

256 mesh refinement is performed if necessary using Cantera’s mesh refinement tools. These
257 steps are repeated until the grid refinement criteria are satisfied and both the gas-phase and
258 solid-phase are converged. The computation of the radiation source term \dot{q}_{rad} from Eq. (9) is
259 done using Eigen’s direct sparse linear solvers. The supplementary materials give additional
260 information regarding the selection of appropriate initial conditions.

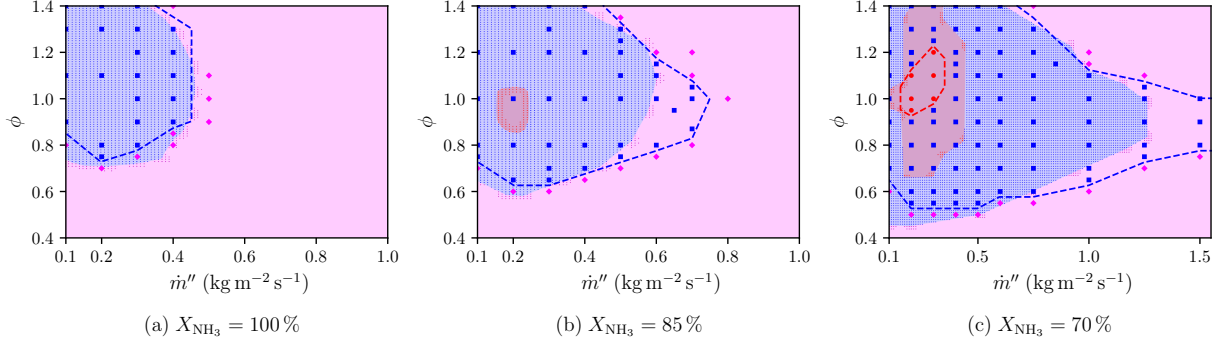
261 4. Results

262 4.1. Stability limits

263 The stability limits of the PMB were experimentally characterized for three different fuel
264 compositions ($X_{\text{NH}_3} = \{100\%, 85\%, 70\%\}$, with H_2 as balance), as a function of equivalence
265 ratio ϕ and mass flux rate \dot{m}'' [56]. Here, stability denotes the stable operation of the
266 burner, where the flame is stabilized at the YZA-SiC interface, and remains as such. In the
267 experiment, this is assessed using thermocouples, whose temperature cannot vary by more
268 than 10 K over 2-min for the condition to be classified as stable. In the simulation, this is
269 assessed by the convergence to a steady-state solution in which the flame is stabilized at
270 the YZA-SiC interface (zero-gradient of temperature at the inlet, peak heat release rates
271 between $25 \text{ mm} < x < 75 \text{ mm}$). Unstable states refer to conditions of either blowoff of the
272 flame (extinction solution in the simulation, $\max(T) < 350 \text{ K}$) or flashback of the flame into
273 the YZA foam (inlet-stabilized solution in the simulation, identified by non-zero temperature
274 gradients at the inlet and peak heat release rates located at $x < 25 \text{ mm}$).

275 Predicting the correct stability behavior requires an accurate description of the flame
276 behavior, of the inter-phase heat exchange processes, and—most importantly—of heat recir-
277 culation. In PMBs, the latter is one of the main processes determining the location at which
278 the flame stabilizes. Accurate predictions require the modeling of radiative heat transfer
279 and heat conduction through the solid matrix. In the following, we present results obtained
280 using the 1D-VAS-FP framework described in Secs. 3. Then, in Sec. 4.2, we will compare
281 the results of the 1D-VAS-FP and 1D-VAS-EMP modelling framework, thereby assessing the
282 importance of accurate determination of effective properties used in closure models.

Simulations conducted using the 1D-VAS-FP framework (Table 5 and Sections 3 and 4.1).



Simulations conducted using the 1D-VAS-EMP framework (Table 6 and Section 4.2).

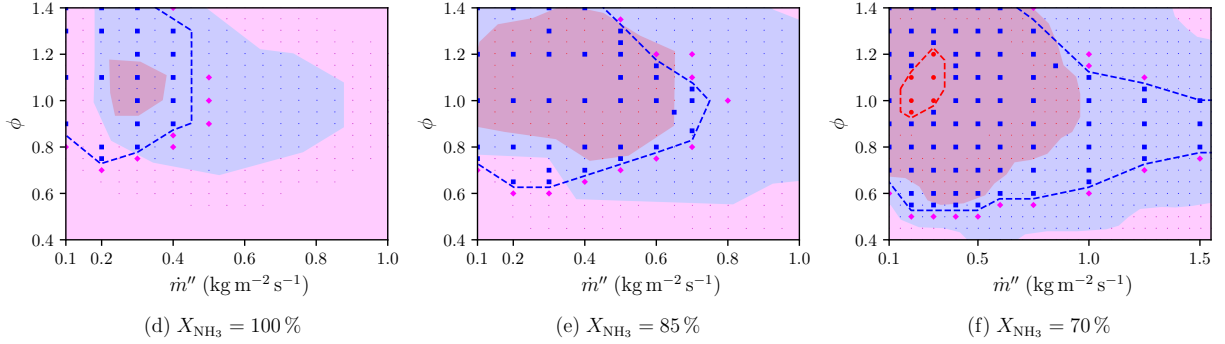


Figure 5: Stability maps as a function of mass flux rate, \dot{m}'' , and equivalence ratio, ϕ , from experiments and simulations. Stable burning conditions are represented by the blue regions (simulations) and blue squares (experiments), blowoff by magenta areas (simulations) and magenta diamonds (experiments), and flashback by red areas (simulations) and red circles (experiments). Blue dashed curves mark the stability limits from the experiments. The small dots mark the conditions for which simulations were conducted. (a,d) $X_{\text{NH}_3} = 100\%$; (b,e) $X_{\text{NH}_3} = 85\%$; and (c,f) $X_{\text{NH}_3} = 70\%$. Top row: 1D-VAS-FP framework; bottom row: 1D-VAS-EMP framework.

283 Figures 5(a-c) compare the stability maps from experiments and from the 1D-VAS-FP
 284 simulations. For $X_{\text{NH}_3} = 100\%$ (Fig. 5(a)), the predicted stability map agrees well with the
 285 measurements. All measured conditions for stable operation (blue squares) lie within the
 286 stable range predicted by the model (blue area). For $X_{\text{NH}_3} = 85\%$ (Fig. 5(b)), good agree-
 287 ment for most conditions is found as well. The stable operation range in the experiments

288 extends to slightly higher mass flux rates for near-stoichiometric conditions. At these high
 289 flow rates, it is likely that multidimensional effects such as flame front wrinkling, stretch,
 290 and local extinctions are present, leading to a thickening of the flame front and a decrease in
 291 combustion efficiency [29, 82, 83]. The 1D volume-averaged model is unable to capture such
 292 effects, which might explain the deviation between the simulation and experiments. Further-
 293 more, the model predicts a small flashback region around $\phi = 0.9$ and $\dot{m}'' = 0.2 \text{ kg m}^{-2} \text{ s}^{-1}$.
 294 Such flashback behavior has been observed experimentally for higher H_2 contents [8, 56]
 295 and the reason for the existence of these flashback regions within otherwise stable operating
 296 conditions is discussed in [56].

297 Lastly, for $X_{\text{NH}_3} = 70\%$ (Fig. 5(c)), the differences between measurements and model
 298 predictions are more pronounced. Following the trend of the $X_{\text{NH}_3} = 85\%$ case, the stable
 299 operation range extends to higher mass flux rates in the experiments compared to the simu-
 300 lations. Furthermore, the predicted stability range from the simulations extends to slightly
 301 leaner conditions at low mass flux rates. The largest difference between measurements and
 302 simulations is the over-prediction of the flashback conditions. While a flashback region is
 303 present in both the experiments (red dashed curves) and the simulations (red area), it is
 304 much more pronounced in simulations, extending up to $\phi = 1.4$ and also to slightly higher
 305 mass flux rates.

To quantify the agreement of the stability maps between simulations and experiments
 more rigorously, we employ the Jaccard index J , given as [84]

$$J = \frac{A_{\text{Exp}} \cap A_{\text{Sim}}}{A_{\text{Exp}} \cup A_{\text{Sim}}}, \quad (16)$$

306 which is formally defined as the area of the intersection of the experimental and simulation
 307 data (area of correctly identified stable or unstable region), divided by the union of the areas
 308 spanned by all experimental and simulation data (all states). Here, we consider the discrete
 309 Jaccard index, which is the sum of all correctly predicted data points divided by all data
 310 points. For the cases with $X_{\text{NH}_3} = 100\%$ (Fig. 5(a)), the model is able to predict 89.6% of
 311 experimentally characterized conditions correctly. For $X_{\text{NH}_3} = 85\%$ cases (Fig. 5(b)), the
 312 simulations are able to correctly classify 74.0% of the stability map. For the $X_{\text{NH}_3} = 70\%$

313 case (Fig. 5(c)), the Jaccard index is 64.1%, which is mainly due to the overprediction of
 314 the flashback region. Nonetheless, the lean blowoff limit is still quantitatively well predicted,
 315 even for case $X_{\text{NH}_3} = 70\%$.

316 Figure 6 provides further quantification of the model accuracy in terms of confusion
 317 matrices. The confusion matrix is used to assess model prediction quality by comparing
 318 ground truth values (here experimental data points) with predicted values (here simulation
 319 results) and are for example commonly used in machine learning applications [54]. For
 320 each experimental measurement point in Fig. 5, the total number of correctly predicted
 321 stable operating conditions (true positives, TP), the number of correctly predicted unstable
 322 conditions (true negatives, TN), and wrongly predicted stable conditions (false positives,
 323 FP) and wrongly predicted unstable conditions (false negatives, FN) are graphically shown
 324 in Fig. 6. The Jaccard index is repeated below each corresponding confusion matrix.

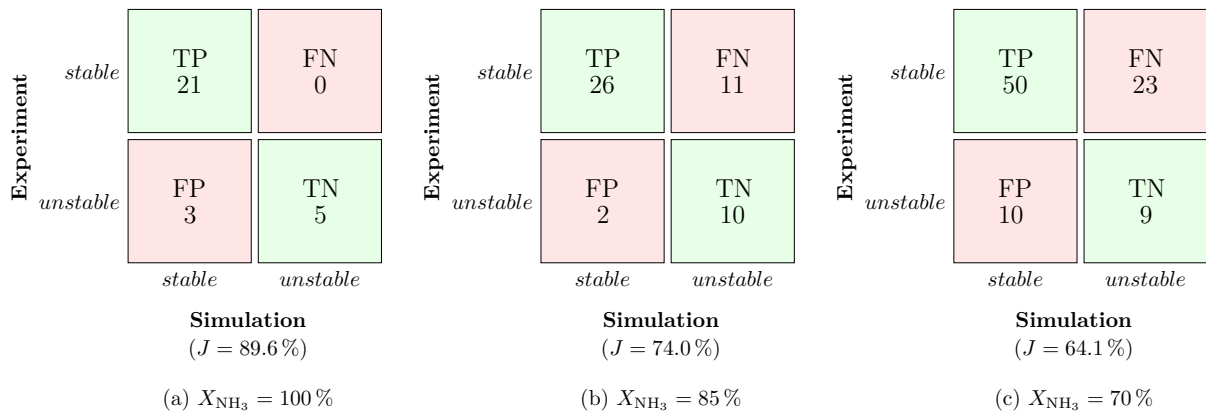


Figure 6: Confusion matrices for the predicted stability maps, for the three cases reported in Fig. 5(a–c).

325 4.2. Direct measurements vs. empirical correlations for constitutive relations and effective 326 properties

327 As shown in Sec. 3.3 and Table 5, all effective properties of the porous matrix have been
 328 determined in this work from first principles, that is from direct 3D measurements of the
 329 porous materials used in the burner, as part of the 1D–VAS–FP framework. The material

330 bulk heat conductivities are however based on literature data. To demonstrate the utility of
 331 this approach, the simulations have been repeated using the 1D-VAS-EMP framework, that
 332 is to say by replacing constitutive relations and effective properties with values derived from
 333 commonly employed empirical correlations. Table 1 summarizes the differences in closure
 334 models between the frameworks. Table 6 summarizes these changes for two crucial effective
 335 properties, the radiative extinction coefficient β and the thermal conductivity efficiency
 336 factor Ξ_{cd} . The main differences between the 1D-VAS-EMP and 1D-VAS-FP framework are:

- 337 i. The extinction coefficient β is computed from an empirical correlation by Bidi et al. [31];
- 338 ii. The efficiency factor for the thermal conductivity of the solid is computed as $\Xi_{\text{cd}} = 1 - \varepsilon_v$;
- 339 iii. Instead of the Schuster-Schwarzschild model, the simpler Rosseland radiation model is
 340 used, where the radiative heat flux is computed as $\dot{q}_{\text{rad}} = -16\sigma T_s^3 / (3\beta) \nabla T_s$ [35];
- 341 iv. Tortuosity effects are neglected ($\eta = 1$).

342 Using a common empirical correlation, the extinction coefficient β is up to ten times smaller
 343 than the value estimated using first-principle measurements. In addition, the heat con-
 344 ductivity in the solid is up to three times higher. To provide a fair comparison, all input
 345 parameters for the empirical models, i.e., bulk material heat conductivities and porosities,
 346 are set to the same values as those used in the 1D-VAS-FP framework.

Table 6: Comparison of effective properties used for the extinction coefficient β and thermal conductivity efficiency factor Ξ_{cd} in the 1D-VAS-FP and 1D-VAS-EMP frameworks.

Quantity	1D-VAS-FP framework			1D-VAS-EMP framework		
	YZA 40 PPI	SiC 3 PPI	SiC 10 PPI	YZA 40 PPI	SiC 3 PPI	SiC 10 PPI
β (m^{-1})	measured			$\beta = 3 \frac{\text{PPI}}{0.0254} (1 - \varepsilon_v)$ [31]		
	1340	526	683	827	49	165
Ξ_{cd} (%)	measured			$\Xi_{\text{cd}} = 1 - \varepsilon_v$		
	7.2	5.1	4.3	17.5	13.9	14.0

347 Figure 5(d-f) shows stability maps obtained with the 1D-VAS-EMP framework. In
 348 all cases, lean blowoff limits are significantly over-predicted, while the upper blowoff limit

Table 7: Jaccard index J corresponding to the stability maps of Fig. 5(a-c) and Fig. 5(d-f).

	1D-VAS-FP	1D-VAS-EMP
X_{NH_3}	(Fig. 5(a-c))	(Fig. 5(d-f))
100 %	89.6 %	44.8 %
85 %	74.0 %	32.7 %
70 %	64.1 %	29.0 %

349 extends to far higher mass flux rates than observed in the experiments. Similarly, the
 350 flashback regions are largely over-predicted as well, appearing for $X_{\text{NH}_3} = 85\%$ (Fig. 5(e))
 351 and even $X_{\text{NH}_3} = 100\%$ (Fig. 5(d)). Using the Jaccard index (Eq. (16)), a quantitative
 352 comparison between the modeling approaches is reported in Table 7.

353 Figure 7 compares two flames computed using the 1D-VAS-FP (red) and 1D-VAS-EMP
 354 (blue) framework. The operating conditions for both simulations are $X_{\text{NH}_3} = 100\%$, $\phi = 0.9$,
 355 and $\dot{m}'' = 0.2 \text{ kg m}^{-2} \text{ s}^{-1}$. Due to the higher heat conductivity of the solid in the 1D-VAS-
 356 EMP simulations (larger thermal conductivity efficiency factor, Ξ_{cd} , and lower extinction
 357 coefficient, β), the flame is pre-heated more effectively, leading to a broader pre-heat zone
 358 that extends far into the YZA section. This effect explains the extended blowoff limits and
 359 higher propensity to flashback obtained with 1D-VAS-EMP. Figure 7(b) shows the axial
 360 radiative heat transport from the Schuster-Schwarzschild model with measured extinction
 361 coefficient (1D-VAS-FP, red curve) and from the Rosseland model with extinction coefficient
 362 estimated from a correlation (1D-VAS-EMP, blue curve). The Rosseland model predicts
 363 higher heat losses in the exhaust gases, leading to lower peak temperatures for the gas and
 364 solid phase at the location of the flame.

365 4.3. Pollutant emissions

366 Figure 8 compares the NO emissions from the measurements and corresponding simula-
 367 tions for $X_{\text{NH}_3} = 100\%$ (Fig. 8(a)) and $X_{\text{NH}_3} = 85\%$ (Fig. 8(b)) as a function of equivalence
 368 ratio for different mass flux rates. Due to the overprediction of flashback at $X_{\text{NH}_3} = 70\%$,
 369 no exhaust gas measurements can be compared with the simulations. The NO formation

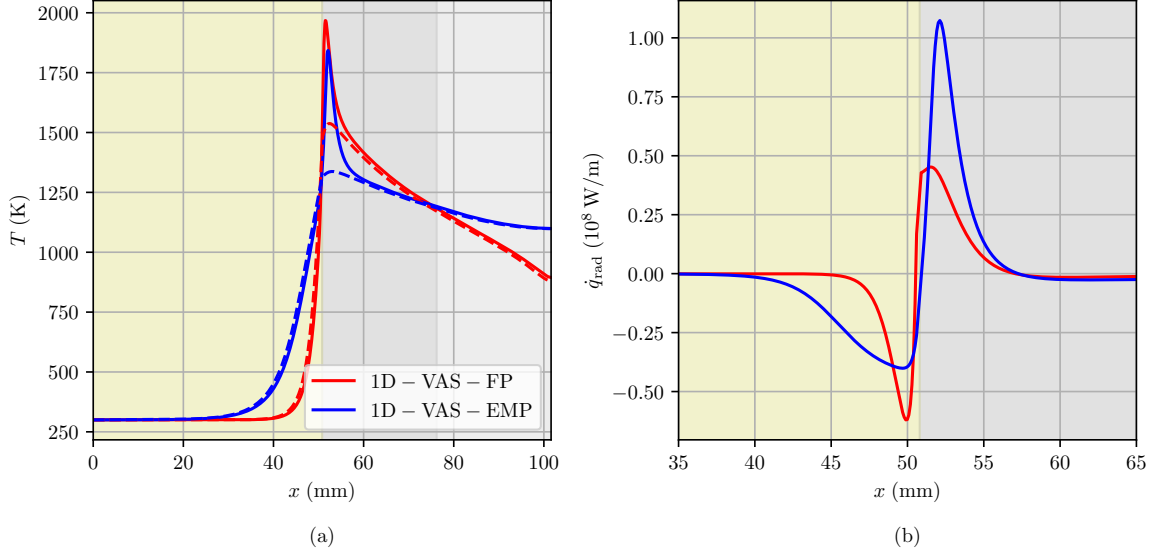


Figure 7: Profiles of (a) gaseous temperature (solid curves) and solid temperature (dashed curves) and (b) axial radiative heat source term for $X_{\text{NH}_3} = 100\%$, $\phi = 0.9$, and $\dot{m}'' = 0.2 \text{ kg m}^{-2} \text{ s}^{-1}$. Red curves are results from simulations conducted within the 1D-VAS-FP framework and blue curves from simulations conducted within the 1D-VAS-EMP framework. Yellow shaded region shows the YZA section of the burner, gray shaded section the 3 PPI and 10 PPI SiC sections.

370 rate is generally sensitive to the peak temperature in the super-adiabatic region of the flame
 371 [1, 2]. Thus, the accurate modeling of both heat conduction and radiative heat transfer in
 372 the solid is required to obtain a correct estimate for NO emission levels. For $X_{\text{NH}_3} = 85\%$
 373 (Fig. 8(b)), the predicted NO levels (red and blue curves) lie mostly within the experimental
 374 uncertainties (blue and red shaded regions). For the $X_{\text{NH}_3} = 100\%$ case (Fig. 8(a)), the
 375 simulations overpredict NO emissions at lean conditions, where experiments have the largest
 376 uncertainties, but still capture the correct trend.

377 Figure 9 compares measurements of unburnt NH_3 in the exhaust gas with the simulation
 378 results. The lower detection limit for experimental measurements lies at about 10 ppmv.
 379 Again, for $X_{\text{NH}_3} = 85\%$ at $\dot{m}'' = 0.3 \text{ kg m}^{-2} \text{ s}^{-1}$, all predicted unburnt NH_3 emission levels
 380 that are above the detection limits of the experiment fall within 25% of the experimental

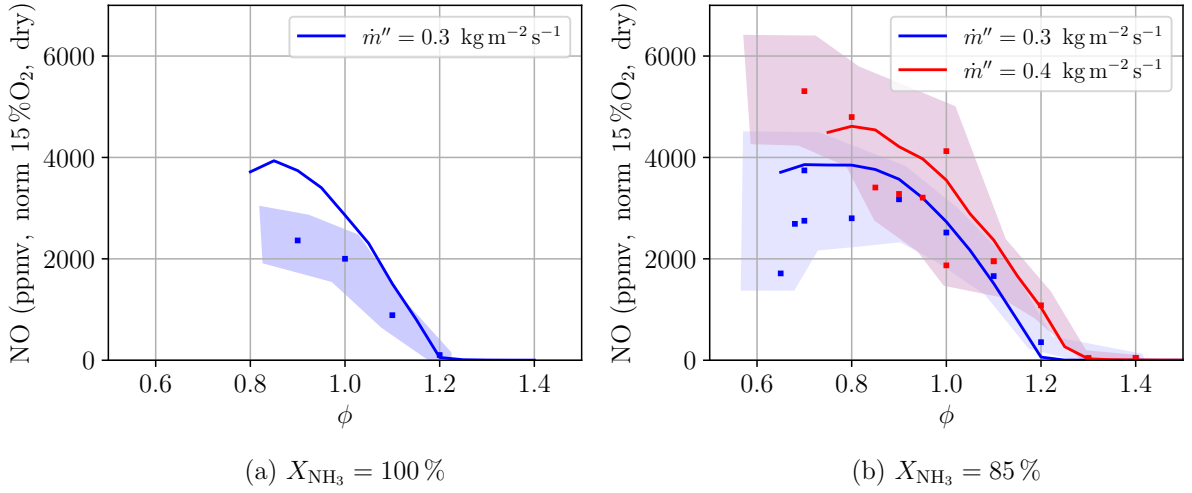


Figure 8: Measured and simulated NO emissions as a function of equivalence ratio, ϕ , for different values of mass flux rates, \dot{m}'' . Solid lines show the simulation results, symbols the experimental measurements, and the shaded regions show the experimental uncertainties.

381 uncertainties. For $\dot{m}'' = 0.4 \text{ kg m}^{-2} \text{ s}^{-1}$, emission levels are underpredicted by 25% for data
 382 points above the detection limit of the experiment. Finally, for $X_{\text{NH}_3} = 100\%$, only one
 383 experimental data point above the detection limit of unburnt NH_3 is available, which is
 384 underpredicted by the simulation as well.

385 Unburnt H_2 was also measured experimentally. It arises from either unburnt H_2 fuel
 386 or from NH_3 pyrolysis. The results are reported in Fig. 10. Experimental measurements
 387 were only performed for $\dot{m}'' = 0.3 \text{ kg m}^{-2} \text{ s}^{-1}$. Again, the predicted H_2 emission levels
 388 for the $X_{\text{NH}_3} = 85\%$ case lie close to the upper limit of the experimental uncertainties
 389 (shaded regions). Consistent with the unburnt NH_3 predictions, H_2 emission levels for the
 390 $X_{\text{NH}_3} = 100\%$ case are under-predicted by about 25%.

391 In summary, the predicted emission levels are within 25% of the measurements for most
 392 conditions reported here. Larger discrepancies are found for unburnt NH_3 emissions at
 393 certain conditions. This shows that the underlying physical phenomena of heat recirculation
 394 stabilizing the flame at the YZA-SiC interface within the PMB are correctly captured by
 395 the model. Trends are also well predicted in all cases.

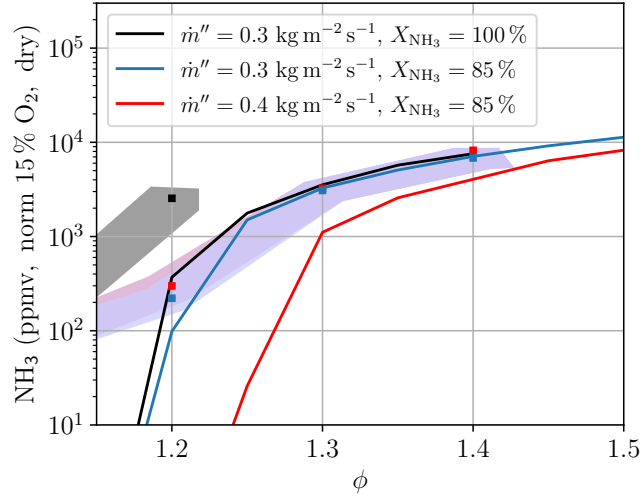


Figure 9: Measured and simulated unburnt NH_3 emissions as a function of equivalence ratio and different values of mass flux rates. Solid curves show the simulations, symbols the experimental measurements, and the shaded regions show the experimental uncertainties.

396 4.4. Effects of operating conditions on pollutant emissions

397 This section investigates the influence of operating conditions on pollutant formation and
 398 flame structure. In what follows, all simulations were conducted within 1D-VAS-FP. Fig-
 399 ure 11 shows the emissions of NO (Fig. 11(a-c)), N_2O (Fig. 11(d-f)), unburnt H_2 (Fig. 11(g-
 400 i)), and unburnt NH_3 (Fig. 11(j-l)) as a function of mass flux rate and equivalence ratio for
 401 different X_{NH_3} fuel composition. NO emissions present a maximum around $0.8 < \phi < 1.0$,
 402 and decrease rapidly under rich conditions. NO emissions also decrease at very lean con-
 403 ditions, around $\phi \approx 0.5$, when flames can be stabilized at such lean conditions. The de-
 404 pendency of NO emissions on mass flux rate is non-monotonic: NO emissions most often
 405 increase rapidly with mass flux, up to a maximum ($\dot{m}'' \approx 0.7 \text{ kg m}^{-2} \text{ s}^{-1}$), after which it
 406 slowly decreases until blowoff occurs. As hydrogen enrichment of the fuel allows the burner
 407 to be operated with higher mass flux rates, the globally highest NO emissions appear for
 408 $X_{\text{NH}_3} = 70\%$. N_2O emissions generally decrease with increasing \dot{m}'' . The highest N_2O emis-
 409 sions occur in the very lean region. This is similar to what is observed for swirl-stabilized
 410 burners [85]. For unburnt H_2 (Fig. 11(g-i)) and NH_3 (Fig. 11(j-l)), the highest concentra-

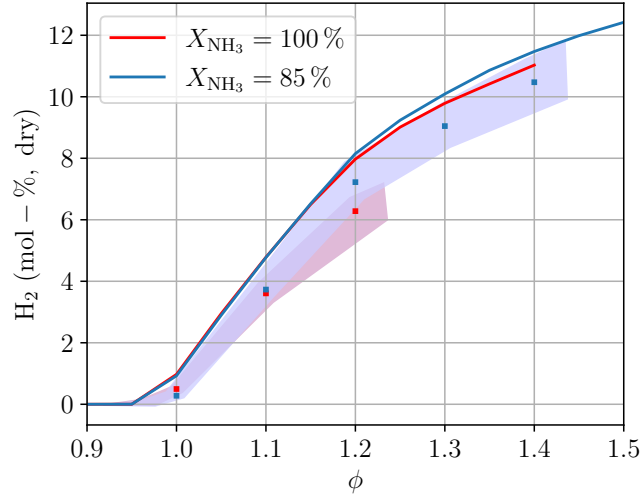


Figure 10: Measured and simulated unburnt H_2 emissions as a function of equivalence ratio and X_{NH_3} at $\dot{m}'' = 0.3 \text{ kg m}^{-2} \text{ s}^{-1}$. Solid lines show the simulation results, symbols the experimental measurements, and shaded regions the experimental uncertainties.

411 tions in the exhaust gas occur at rich operating conditions. There is a marked decrease
 412 in unburnt NH_3 with increasing \dot{m}'' , indicating higher NH_3 cracking efficiency within the
 413 burner. These observations are in good agreement with experimental results [8, 56].

414 The reason for the change of pollutant emissions with mass flux rate is studied in Fig. 12
 415 for $\phi = 0.9$ and mass flux rates $\dot{m}'' \in \{0.1, 0.2, 0.3\} \text{ kg m}^{-2} \text{ s}^{-1}$. Figure 12(a) shows the
 416 temperature profiles of three flames at $\phi = 0.9$ and $X_{\text{NH}_3} = 100\%$ for different mass flux
 417 rates. The flame is in all cases stabilized at the interface between the YZA section of
 418 the burner (yellow shaded region) and the 3 PPI SiC section (gray shaded region). As
 419 the mass flux rate increases, the volumetric heat release rate correspondingly increases,
 420 leading to higher temperatures. Therefore, both the peak gas-phase temperatures (solid
 421 curves) and the peak solid-phase temperatures (dashed curves) increase with \dot{m}'' . For the
 422 low mass flux case, the flame is considerably broadened and peak temperatures are below
 423 the adiabatic flame temperature (horizontal dotted line) due to heat losses in the burner.
 424 Consequently, NO emissions increase with increasing mass flux rate (Fig. 12(b)), due to the
 425 strong temperature dependence of NO formation pathways [1]. A more detailed analysis is

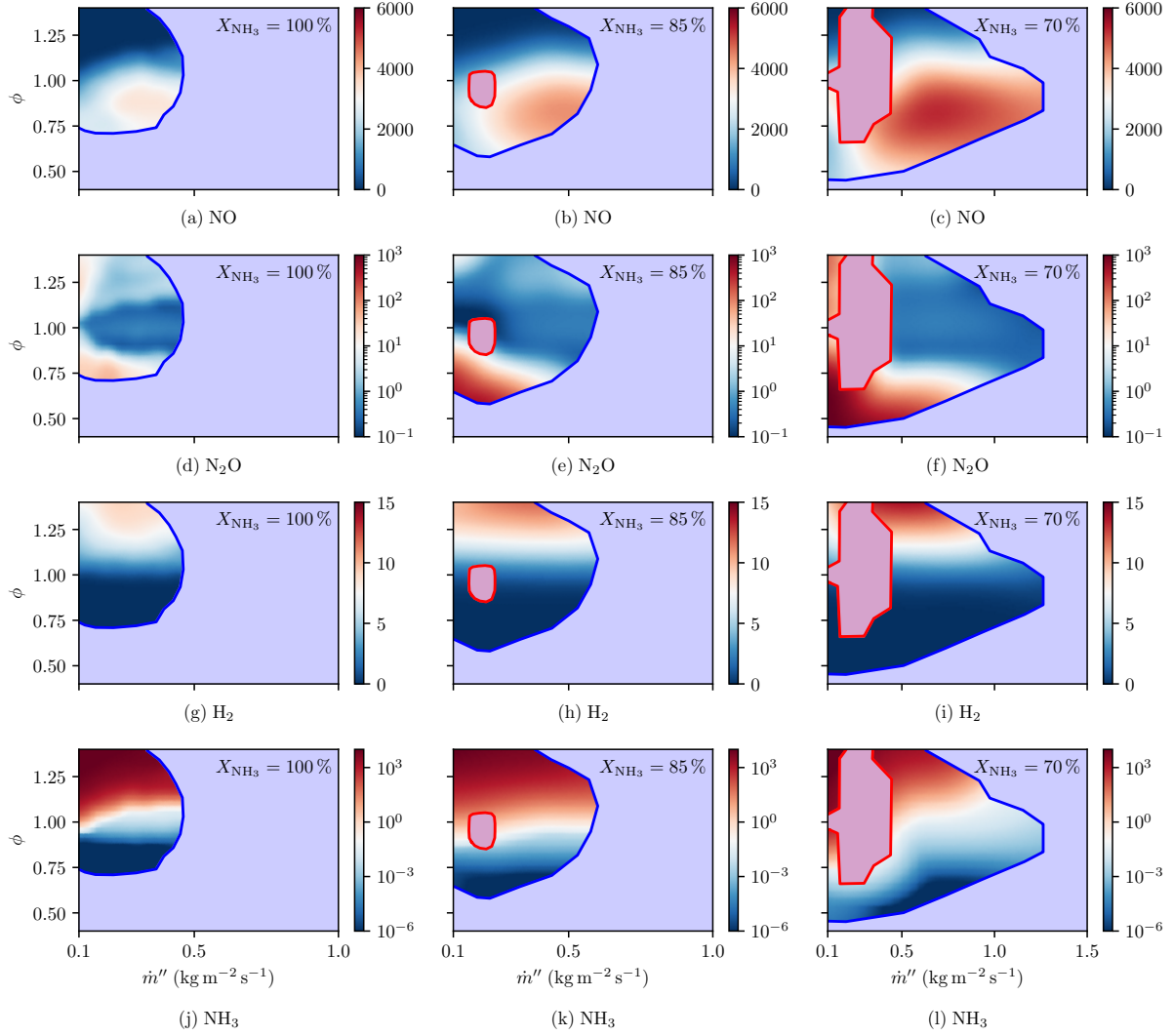


Figure 11: Emissions of NO (a–c), N_2O (d–f), unburnt H_2 (g–i) and unburnt NH_3 (j–l) as a function of equivalence ratio and mass flux rate for different X_{NH_3} . All emissions, except unburnt H_2 , are reported in ppmv, normalized to 15% O_2 , dry. H_2 emissions are given in mol-%, dry. The blue curve marks the blowoff limit and the red shaded area the flashback region.

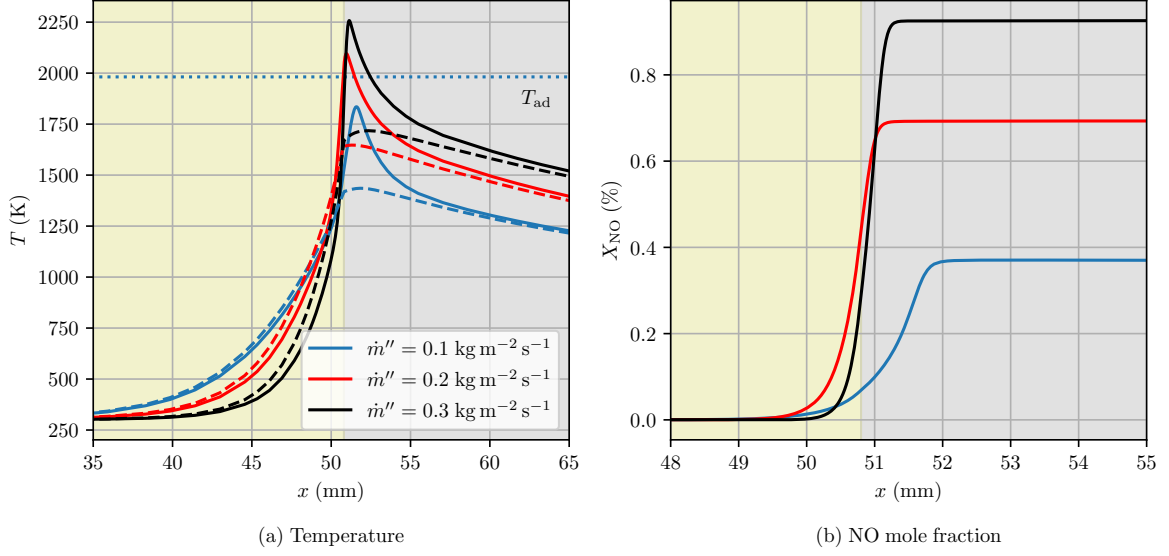


Figure 12: Profiles of (a) gaseous temperature (solid curves) and solid temperature (dashed curves) and (b) NO mole fraction for $X_{\text{NH}_3} = 100\%$ and $\phi = 0.9$ at different mass flux rates \dot{m}'' . Yellow shaded region shows the YZA section of the burner and gray shaded region shows the 3 PPI SiC section. The dotted line marks the adiabatic flame temperature.

426 given in the supplementary materials.

427 Maximum N_2O emissions are found at lean conditions at sub-adiabatic temperatures,
 428 where N_2O is formed preferentially due to lower competition from NO formation. Similarly,
 429 the highest unburnt NH_3 emissions are found at rich conditions and at the coldest temper-
 430 atures, which kinetically limits the decomposition process of NH_3 . Inversely, the highest H_2
 431 levels are found at rich operating conditions and high flow rates, where the highest super-
 432 adiabatic temperatures are reached and where thermal cracking of NH_3 into H_2 is most
 433 intense.

434 The dependence of the peak temperature on operating conditions is depicted in Fig. 13(a-
 435 c) in terms of the difference between the peak gas-phase temperature inside the burner and
 436 the corresponding adiabatic flame temperature. With increasing mass flux rates, peak tem-
 437 peratures increase and the burner operates in the super-adiabatic regime. For low mass flux
 438 rates, peak temperatures stay below the adiabatic flame temperature. Peak temperatures

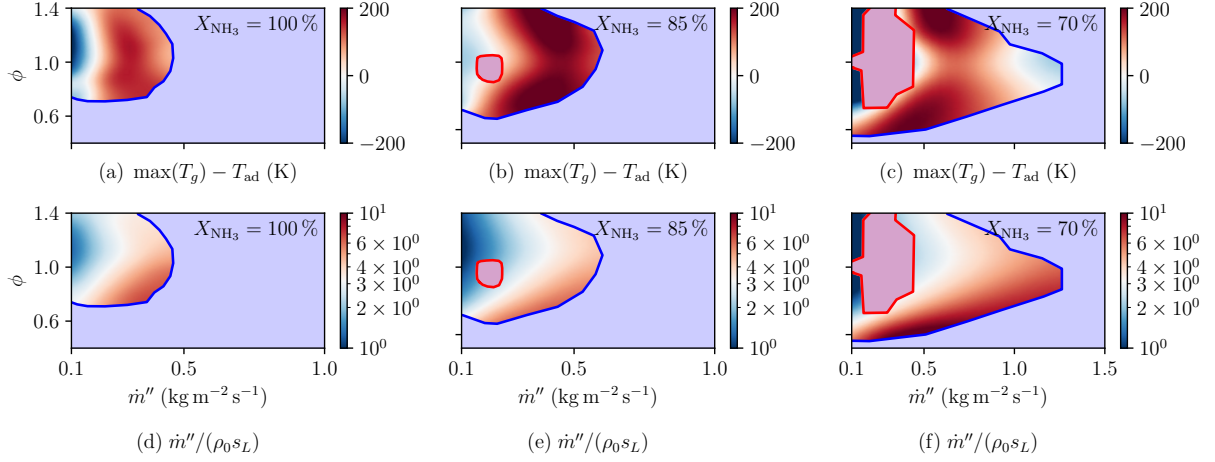


Figure 13: (a–c): difference between the peak gas-phase temperature and adiabatic flame temperature $\max(T_g) - T_{\text{ad}}$. The red regions correspond to super-adiabatic combustion; (d–f): ratio of burner mass flux rate to the mass flux rate of a corresponding adiabatic freely propagating flame, $\dot{m}''/(\rho_0 s_L)$, where ρ_0 is the density of the unburnt gas and s_L is the adiabatic flame speed, as a function of equivalence ratio and mass flux rate for different X_{NH_3} . The blue curve marks the blowoff limit and the red shaded area indicates the flashback region.

439 also tend to decrease near the stoichiometric upper blowoff limit.

440 Figure 13(d–f) compares the mass flux rate of the burner, where stable operation can be
 441 achieved, with the corresponding mass flux rate of an adiabatic, freely propagating laminar
 442 flame, as a function of ϕ . For pure NH_3 flames, mass flux rates can be increased by a factor of
 443 six due to the internal heat recirculation and stabilization of the burner. For $X_{\text{NH}_3} = 70\%$, a
 444 tenfold increase is achieved. This increase towards stable operation at high mass flux rates,
 445 and the correspondingly high volumetric power densities, highlights the ability of PMBs to
 446 compensate for the generally low flame speeds of NH_3 in practical applications.

447 5. Conclusions

448 The present work focuses on 1D volume-averaged simulations of matrix stabilized com-
 449 bustion, with application to the combustion of premixed NH_3/H_2 -air blends in an interface-

450 stabilized PMB. We propose a cohesive open-source simulation framework, referred to as
451 1D-VAS-FP, in which the parameters for closure models used for 1D volume-averaged simula-
452 tions are derived from first-principle simulations conducted on geometries directly extracted
453 from μ CT scans of the open-cell ceramic foams used in the burner. These properties include
454 tortuosity, effective heat conductivity of the solid phase, and radiative extinction coefficient.
455 The results show that the 1D-VAS-FP simulations compare well with measurements in terms
456 of stability limits and exhaust gas composition when adequately determined effective prop-
457 erties are utilized. In contrast, when using empirical correlations found in the literature,
458 volume-averaged simulations can no longer be considered as predictive. This demonstrates
459 that volume-averaged models enable reliable predictions when utilizing constitutive mod-
460 els and effective properties derived from well-characterized geometries using first-principles
461 methods—particularly when dealing with emerging fuels with challenging combustion prop-
462 erties. Regarding the capabilities of the 1D-VAS-FP modeling framework, the conclusions of
463 this work are summarized as follows:

- 464 i. Using effective properties estimated from first-principle simulations together with the
465 Schuster-Schwarzschild radiation model, predicted emissions of NO, unburnt NH₃ and
466 H₂ are within 25 % of the measurement uncertainties for most conditions, and experi-
467 mental results are correctly reproduced;
- 468 ii. The 1D-VAS-FP modeling framework yields reliable stability limits for the burner. For
469 operation with pure NH₃, 90 % of all measured conditions are correctly captured by the
470 1D volume-averaged model. While blowoff limits are generally well predicted, flashback
471 for high H₂ dilution is overpredicted. The high-velocity blow-off limit is also overpre-
472 dicted, most likely due to flame wrinkling in this regime;
- 473 iii. At the same conditions, when utilizing closure models based on empirical correlations
474 (1D-VAS-EMP), simulations are unreliable and largely overpredict blowoff and flashback
475 limits. This is attributed to the much higher effective heat conductivity of the solid,
476 leading to a much broader pre-heat region that extends into the flame arrestor integrated
477 in the burner.

478 A limitation of this approach is that detailed geometric information of the porous matrix
479 are required. These can typically be obtained using commonly available μ CT, or, during
480 the design phase of a PMB, using modern computer-assisted design tools. The availability
481 of accurate bulk thermal properties for engineered ceramic materials used in PMB can also
482 be an issue for predictive simulations [36].

483 Regarding the flame anchoring mechanism and pollutant formation in matrix-stabilized
484 NH_3/H_2 -air flames, the following conclusions were reached:

485 iv. At low mass flux rates, the peak gas-phase temperatures are below the adiabatic flame
486 temperatures, leading to a broadening of the flame front inside the porous matrix. For
487 most conditions within the stable operating range, peak temperatures exceed T_{ad} due
488 to the internal heat recirculation, enabling super-adiabatic combustion.

489 v. Due to the effect of mass flux rates on peak temperatures, low mass flow rates result in
490 lower NO and higher N_2O formation at lean conditions. At rich conditions, the lower
491 solid temperatures at low mass flow rates result in higher unburnt NH_3 and lower H_2
492 emissions.

493 vi. Flame speeds can be increased tenfold in the PMB, which demonstrates that PMC can
494 compensate for the low flame speed of NH_3 and yield high volumetric power densities.

495 The simulation code for 1D volume-averaged porous media combustion developed in this
496 work is implemented in Cantera and publicly available [66].

497 **Acknowledgments**

498 T. Zirwes and D. Trimis acknowledge the support of the PRIME program of the German
499 Academic Exchange Service (DAAD) with funds from the German Federal Ministry of Edu-
500 cation and Research (BMBF). E. Boigné was supported by the National Science Foundation
501 with Award No. CBET-1800906. K. Younes gratefully acknowledges financial support from
502 the U.S. Department of Energy, Office of Science under DOE (BES) Award DE-SC0022222.
503 Part of this work was performed at the Stanford Nano Shared Facilities (SNSF), supported
504 by the National Science Foundation under award ECCS-2026822. The authors thank Joseph

505 C. Ferguson for helpful discussion on the utilization and extension of the PuMA analysis
506 software.

507 References

- 508 [1] A. Valera-Medina, F. Amer-Hatem, A. K. Azad, I. C. Dedoussi, M. de Joannon, R. X. Fernandes,
509 P. Glarborg, H. Hashemi, X. He, S. Mashruk, J. McGowan, C. Mounaim-Rouselle, A. Ortiz-Prado,
510 A. Ortiz-Valera, I. Rossetti, B. Shu, M. Yehia, H. Xiao, M. Costa, Review on ammonia as a potential
511 fuel: From synthesis to economics, *Energ. Fuel* 35 (2021) 6964–7029.
- 512 [2] H. Kobayashi, A. Hayakawa, K. D. A. Somarathne, E. C. Okafor, Science and technology of ammonia
513 combustion, *Proc. Combust. Inst.* 37 (2019) 109–133.
- 514 [3] L. Pizzuti, C. A. Martins, P. T. Lacava, Laminar burning velocity and flammability limits in biogas:
515 A literature review, *Renew. Sustain. Energy Rev.* 62 (2016) 856–865.
- 516 [4] J. L. Ellzey, E. L. Belmont, C. H. Smith, Heat recirculating reactors: Fundamental research and
517 applications, *Prog. Energ. Combust. Sci.* 72 (2019) 32–58.
- 518 [5] D. Trimis, F. Durst, Combustion in a porous medium: Advances and applications, *Combust. Sci.*
519 *Technol.* 121 (1996) 153–168.
- 520 [6] M. A. Mujeebu, M. Z. Abdullah, A. Mohamad, M. A. Bakar, Trends in modeling of porous media
521 combustion, *Prog. Energ. Combust. Sci.* 36 (2010) 627–650.
- 522 [7] H. Nozari, G. Karaca, O. Tuncer, A. Karabeyoglu, Porous medium based burner for efficient and clean
523 combustion of ammonia–hydrogen–air systems, *Int. J. Hydrog. Energ.* 42 (2017) 14775–14785.
- 524 [8] G. Vignat, B. Akoush, E. R. Toro Garza, E. Boigné, M. Ihme, Combustion of lean ammonia-hydrogen
525 fuel blends in a porous media burner, *Proc. Combust. Inst.* 39 (2023) 4195–4204.
- 526 [9] D. Chen, J. Li, X. Li, L. Deng, Z. He, H. Huang, N. Kobayashi, Study on combustion characteristics
527 of hydrogen addition on ammonia flame at a porous burner, *Energy* 263 (2023) 125613.
- 528 [10] C. Keramiotis, M. Katoufa, G. Vourliotakis, A. Hatzia Apostolou, M. A. Founti, Experimental investiga-
529 tion of a radiant porous burner performance with simulated natural gas, biogas and synthesis gas fuel
530 blends, *Fuel* 158 (2015) 835–842.
- 531 [11] F. Song, Z. Wen, Z. Dong, E. Wang, X. Liu, Ultra-low calorific gas combustion in a gradually-varied
532 porous burner with annular heat recirculation, *Energy* 119 (2017) 497–503.
- 533 [12] S. S. Su, S. J. Hwang, W. H. Lai, On a porous medium combustor for hydrogen flame stabilization and
534 operation, *Int. J. Hydrog. Energ.* 39 (2014) 21307–21316.
- 535 [13] A. A. M. Oliveira, M. Kaviany, Nonequilibrium in the transport of heat and reactants in combustion
536 in porous media, *Prog. Energ. Combust. Sci.* 27 (2001) 523–545.

- 537 [14] C. Wieland, C. Weis, P. Habisreuther, D. Trimis, 3D direct pore level simulations of radiant porous
538 burners, *Combust. Flame* 245 (2022) 112370.
- 539 [15] P.-A. Masset, F. Duchaine, A. Pestre, L. Selle, Modelling challenges of volume-averaged combustion in
540 inert porous media, *Combust. Flame* 251 (2023) 112678.
- 541 [16] I. Yakovlev, S. Zambalov, Three-dimensional pore-scale numerical simulation of methane-air combustion
542 in inert porous media under the conditions of upstream and downstream combustion wave propagation
543 through the media, *Combust. Flame* 209 (2019) 74–98.
- 544 [17] S. Sobhani, D. Mohaddes, E. Boigne, P. Muhunthan, M. Ihme, Modulation of heat transfer for extended
545 flame stabilization in porous media burners via topology gradation, *Proc. Combust. Inst.* 37 (2019)
546 5697–5704.
- 547 [18] D. A. Lawson, J. Norbury, Numerical solution of combustion in a porous medium, in: R. W. Lewis,
548 K. Morgan (Eds.), *Numerical Methods in Heat Transfer*, Vol. 3, Wiley New York, 1985, pp. 175–181.
- 549 [19] N. Djordjevic, P. Habisreuther, N. Zarzalis, A numerical investigation of the flame stability in porous
550 burners employing various ceramic sponge-like structures, *Chem. Eng. Sci.* 66 (2011) 682–688.
- 551 [20] G. Brenner, K. Pickenäcker, O. Pickenäcker, D. Trimis, K. Wawrzinek, T. Weber, Numerical and
552 experimental investigation of matrix-stabilized methane/air combustion in porous inert media, *Com-
553 bust. Flame* 123 (2000) 201–213.
- 554 [21] R. S. Dhamrat, J. L. Ellzey, Numerical and experimental study of the conversion of methane to hydrogen
555 in a porous media reactor, *Combust. Flame* 144 (2006) 698–709.
- 556 [22] D. Diamantis, E. Mastorakos, D. Goussis, Simulations of premixed combustion in porous media, *Com-
557 bust. Theor. Model.* 6 (2002) 383.
- 558 [23] S. Sobhani, B. Haley, D. Bartz, J. Dunnmon, J. Sullivan, M. Ihme, Investigation of lean combustion
559 stability, pressure drop, and material durability in porous media burners, in: *Turbo Expo: Power for
560 Land, Sea, and Air*, Vol. 5c, American Society of Mechanical Engineers, 2017, pp. 1–12.
- 561 [24] M. Toledo, V. Bubnovich, A. Saveliev, L. Kennedy, Hydrogen production in ultrarich combustion of
562 hydrocarbon fuels in porous media, *Int. J. Hydrog. Energ.* 34 (2009) 1818–1827.
- 563 [25] A. J. Barra, G. Diepvens, J. L. Ellzey, M. R. Henneke, Numerical study of the effects of material
564 properties on flame stabilization in a porous burner, *Combust. Flame* 134 (2003) 369–379.
- 565 [26] M. Dixon, I. Schoegl, C. Hull, J. Ellzey, Experimental and numerical conversion of liquid heptane to
566 syngas through combustion in porous media, *Combust. Flame* 154 (2008) 217–231.
- 567 [27] M. Sahraoui, M. Kaviany, Direct simulation vs. volume-averaged treatment of adiabatic, premixed
568 flame in a porous medium, *Int. J. Heat Mass Transf.* 37 (1994) 2817–2834.
- 569 [28] J.-R. Shi, C.-M. Yu, B.-W. Li, Y.-F. Xia, Z.-J. Xue, Experimental and numerical studies on the flame
570 instabilities in porous media, *Fuel* 106 (2013) 674–681.

- 571 [29] C. Bedoya, I. Dinkov, P. Habisreuther, N. Zarzalis, H. Bockhorn, P. Parthasarathy, Experimental
572 study, 1D volume-averaged calculations and 3D direct pore level simulations of the flame stabilization
573 in porous inert media at elevated pressure, *Combust. Flame* 162 (2015) 3740–3754.
- 574 [30] R. C. Rocha, C. F. Ramos, M. Costa, X. S. Bai, Combustion of $\text{NH}_3/\text{CH}_4/\text{air}$ and $\text{NH}_3/\text{H}_2/\text{air}$ mixtures
575 in a porous burner: Experiments and kinetic modeling, *Energ. Fuel* 33 (2019) 12767–12780.
- 576 [31] M. Bidi, M. Nobari, M. S. Avval, A numerical evaluation of combustion in porous media by EGM
577 (Entropy Generation Minimization), *Energy* 35 (2010) 3483–3500.
- 578 [32] P. A. Masset, O. Dounia, L. Selle, Fully explicit formulae for flame speed in infinite and finite porous
579 media, *Combust. Theor. Model.* 25 (2021) 785–812.
- 580 [33] M. R. Henneke, J. L. Ellzey, Modeling of filtration combustion in a packed bed, *Combust. Flame* 117
581 (1999) 832–840.
- 582 [34] C. Tseng, Effects of hydrogen addition on methane combustion in a porous medium burner, *Int. J.*
583 *Hydrog. Energ.* 27 (2002) 699–707.
- 584 [35] J. R. Howell, M. P. Mengüç, K. Daun, R. Siegel, *Thermal Radiation Heat Transfer*, CRC Press, 2020.
- 585 [36] S. Sobhani, S. Allan, P. Muhunthan, E. Boigne, M. Ihme, Additive manufacturing of tailored macrop-
586 orous ceramic structures for high-temperature applications, *Adv. Eng. Mater.* 22 (2020) 1–8.
- 587 [37] M. Kaviany, *Principles of Heat Transfer in Porous Media*, Springer Science & Business Media, 2012.
- 588 [38] S. Voss, M. Mendes, J. Pereira, S. Ray, J. Pereira, D. Trimis, Investigation on the thermal flame
589 thickness for lean premixed combustion of low calorific H_2/CO mixtures within porous inert media,
590 *Proc. Combust. Inst.* 34 (2013) 3335–3342.
- 591 [39] M. Mendes, J. Pereira, J. Pereira, Calculation of premixed combustion within inert porous media with
592 model parametric uncertainty quantification, *Combust. Flame* 158 (2011) 466–476.
- 593 [40] X. Fu, R. Viskanta, J. Gore, Prediction of effective thermal conductivity of cellular ceramics, *Int.*
594 *Commun. Heat Mass Transf.* 25 (1998) 151–160.
- 595 [41] J. C. Ferguson, F. Panerai, A. Borner, N. N. Mansour, PuMA: The porous microstructure analysis
596 software, *SoftwareX* 7 (2018) 81–87.
- 597 [42] N. Wakao, S. Kagei, *Heat and Mass Transfer in Packed Beds*, Vol. 1, Taylor & Francis, 1982.
- 598 [43] L. Younis, R. Viskanta, Experimental determination of the volumetric heat transfer coefficient between
599 stream of air and ceramic foam, *Int. J. Heat Mass Transf.* 36 (1993) 1425–1434.
- 600 [44] H. Liu, S. Dong, B.-W. Li, H.-G. Chen, Parametric investigations of premixed methane–air combustion
601 in two-section porous media by numerical simulation, *Fuel* 89 (2010) 1736–1742.
- 602 [45] M. Scheffler, P. Colombo, *Cellular Ceramics: Structure, Manufacturing, Properties and Applications*,
603 John Wiley & Sons, 2006.
- 604 [46] H. T. Hamad, D. W. Abbood, A. S. Mustafa, Strength tortuosity-porosity relation in locally types of

- 605 porous media (experimental model), in: IOP Conference Series: Materials Science and Engineering,
606 Vol. 454, IOP Publishing, 2018, p. 012093.
- 607 [47] S.-Y. Hsu, The effects of tortuosity and dispersion on porous combustion, *Combust. Theor. Model.* 25
608 (2017) 1175–1194.
- 609 [48] F. Kuwahara, M. Shirota, A. Nakayama, A numerical study of interfacial convective heat transfer
610 coefficient in two-energy equation model of porous media, *Int. J. Heat Mass Transf.* 44 (1) 1153–1159.
- 611 [49] R. Habib, N. Karimi, B. Yadollahi, M. H. Doranehgard, L. K. Li, A pore-scale assessment of the
612 dynamic response of forced convection in porous media to inlet flow modulations, *Int. J. Heat Mass*
613 *Transf.* 153 (2020) 119657.
- 614 [50] P. Habisreuther, N. Djordjevic, N. Zarzalis, Statistical distribution of residence time and tortuosity of
615 flow through open-cell foams, *Chem. Eng. Sci.* 64 (2009) 4943–4954.
- 616 [51] A. J. Barra, J. L. Ellzey, Heat recirculation and heat transfer in porous burners, *Combust. Flame* 137
617 (2004) 230–241.
- 618 [52] J. C. Ferguson, A. Borner, F. Panerai, S. Close, N. N. Mansour, Continuum to rarefied diffusive
619 tortuosity factors in porous media from x-ray microtomography, *Comput. Mater. Sci.* 203 (2022) 111030.
- 620 [53] K. M. Graczyk, M. Matyka, Predicting porosity, permeability, and tortuosity of porous media from
621 images by deep learning, *Sci. Rep.* 10 (2020) 21488.
- 622 [54] M. Ihme, W. T. Chung, A. A. Mishra, Combustion machine learning: Principles, progress and prospects,
623 *Prog. Energ. Combust. Sci.* 91 (2022) 101010.
- 624 [55] G. Zhang, Q. Li, X. Liu, B. Lin, X. Li, Numerical investigation on lean methane combustion with
625 modified effective thermal conductivity of the porous media, *Combust. Theor. Model.* 26 (2021) 365–
626 382.
- 627 [56] G. Vignat, T. Zirwes, E. R. Toro Garza, K. Younes, E. Boigné, P. Muhunthan, L. Simitz, D. Trimis,
628 M. Ihme, Experimental and numerical investigation of flame stabilization and pollutant formation in
629 matrix stabilized ammonia-hydrogen combustion, *Combust. Flame* 250 (2023) 112642.
- 630 [57] C. E. Baukal, P. B. Eleazer, Quantifying NO_x for industrial combustion processes, *J. Air Waste Manag.*
631 *Assoc.* 48 (1998) 52–58.
- 632 [58] J. R. Howell, M. J. Hall, J. L. Ellzey, Combustion of hydrocarbon fuels within porous inert media,
633 *Prog. Energ. Combust. Sci.* 22 (1996) 121–145.
- 634 [59] R. J. Kee, M. E. Coltrin, P. Glarborg, *Chemically Reacting Flow: Theory and Practice*, John Wiley &
635 Sons, 2005.
- 636 [60] P.-f. Hsu, J. R. Howell, Measurements of thermal conductivity and optical properties of porous partially
637 stabilized zirconia, *Exp. Heat Transfer* 5 (1992) 293–313.
- 638 [61] M. Pelanconi, M. Barbato, S. Zavattoni, G. Vignoles, A. Ortona, Thermal design, optimization and

- 639 additive manufacturing of ceramic regular structures to maximize the radiative heat transfer, *Materials*
640 & Design 163 (2019) 107539.
- 641 [62] A. Stagni, C. Cavallotti, S. Arunthanayothin, Y. Song, O. Herbinet, F. Battin-Leclerc, T. Faravelli, An
642 experimental, theoretical and kinetic-modeling study of the gas-phase oxidation of ammonia, *React.*
643 *Chem. Eng.* 5 (2020) 696–711.
- 644 [63] X. Zhang, S. P. Moosakutty, R. P. Rajan, M. Younes, S. M. Sarathy, Combustion chemistry of ammo-
645 nia/hydrogen mixtures: Jet-stirred reactor measurements and comprehensive kinetic modeling, *Combust.*
646 *Flame* 234 (2021) 111653.
- 647 [64] San Diego Mechanism, Chemical-kinetic mechanisms for combustion applications: Nitrogen chemistry,
648 <http://combustion.ucsd.edu> (2018).
- 649 [65] D. G. Goodwin, R. L. Speth, H. K. Moffat, B. W. Weber, Cantera: An object-oriented software toolkit
650 for chemical kinetics, thermodynamics, and transport processes, <https://www.cantera.org> (2021).
- 651 [66] Porous media combustion extension for Cantera, <https://github.com/IhmeGroup>, 2023 (repository
652 will be added to the published manuscript).
- 653 [67] M. Kuwahara, K. Hachimura, S. Eiho, M. Kinoshita, Processing of RI-angiocardigraphic images, in:
654 *Digital Processing of Biomedical Images*, Springer, 1976, pp. 187–202.
- 655 [68] N. Otsu, A threshold selection from gray-level histograms, *IEEE Transactions on Systems, Man, and*
656 *Cybernetics SMC-9* (1979) 62–66.
- 657 [69] J. C. Ferguson, F. Semeraro, J. M. Thornton, F. Panerai, A. Borner, N. N. Mansour, Update 3.0
658 to “PuMA: The Porous Microstructure Analysis software”, (PII:S2352711018300281), *SoftwareX* 15
659 (2021) 100775.
- 660 [70] O. Nilsson, H. Mehling, R. Horn, J. Fricke, R. Hofmann, S. G. Müller, R. Eckstein, D. Hofmann,
661 Determination of the thermal diffusivity and conductivity of monocrystalline silicon carbide (300-2300
662 K), *High Temp.-High Press.* 29 (1997) 73–79.
- 663 [71] G. A. Slack, Thermal conductivity of pure and impure silicon, silicon carbide, and diamond, *J. Appl.*
664 *Phys.* 35 (1964) 3460–3466.
- 665 [72] D. M. Liu, B. W. Lin, Thermal conductivity in hot-pressed silicon carbide, *Ceram. Int.* 22 (1996)
666 407–414.
- 667 [73] K. Terrani, B. Jolly, M. Trammell, 3D printing of high-purity silicon carbide, *J. Am. Ceram. Soc.* 103
668 (2020) 1575–1581.
- 669 [74] K. Pelissier, T. Chartier, J. M. Laurent, Silicon carbide heating elements, *Ceram. Int.* 24 (1998) 371–
670 377.
- 671 [75] N. P. Bansal, D. Zhu, Thermal conductivity of zirconia-alumina composites, *Ceram. Int.* 31 (2005)
672 911–916.

- 673 [76] G. Pia, L. Casnedi, U. Sanna, Porosity and pore size distribution influence on thermal conductivity of
674 yttria-stabilized zirconia: Experimental findings and model predictions, *Ceram. Int.* 42 (2016) 5802–
675 5809.
- 676 [77] K. W. Schlichting, N. P. Padture, P. G. Klemens, Thermal conductivity of dense and porous yttria-
677 stabilized zirconia, *J. Mater. Sci.* 36 (2001) 3003–3010.
- 678 [78] E. Maire, P. Colombo, J. Adrien, L. Babout, L. Biasetto, Characterization of the morphology of cellular
679 ceramics by 3D image processing of X-ray tomography, *J. Eur. Ceram. Soc.* 27 (2007) 1973–1981.
- 680 [79] J. Gostick, Z. Khan, T. Tranter, M. Kok, M. Agnaou, M. Sadeghi, R. Jervis, PoreSpy: A Python
681 toolkit for quantitative analysis of porous media images, *J. Open Source Softw.* 4 (2019) 1296.
- 682 [80] R. J. Kee, F. M. Rupley, E. Meeks, J. A. Miller, CHEMKIN-III: A FORTRAN chemical kinetics package
683 for the analysis of gas-phase chemical and plasma kinetics, Tech. rep., Sandia National Laboratories
684 (SNL-CA), Livermore, CA (United States) (1996).
- 685 [81] G. Guennebaud, B. Jacob, et al., Eigen v3, <http://eigen.tuxfamily.org> (2010).
- 686 [82] J. C. Ferguson, S. Sobhani, M. Ihme, Pore-resolved simulations of porous media combustion with
687 conjugate heat transfer, *Proc. Combust. Inst.* 38 (2021) 2127–2134.
- 688 [83] R. V. Fursenko, I. A. Yakovlev, E. S. Odintsov, S. D. Zambalov, S. S. Minaev, Pore-scale flame dynamics
689 in a one-layer porous burner, *Combust. Flame* 235 (2022) 111711.
- 690 [84] A. H. Murphy, The Finley affair: A signal event in the history of forecast verification, *Weather Forecast.*
691 11 (1996) 3–20.
- 692 [85] S. Mashruk, E. Okafor, M. Kovaleva, A. Alnasif, D. G. Pugh, A. Hayakawa, A. Valera-Medina, Evolu-
693 tion of N₂O production at lean combustion condition in NH₃/H₂/air premixed swirling flames, *Com-
694 bust. Flame* 244 (2022) 112299.